nature neuroscience

Article

https://doi.org/10.1038/s41593-024-01824-y

Simultaneous intracranial recordings of interacting brains reveal neurocognitive dynamics of human cooperation

Received: 13 October 2023

Accepted: 17 October 2024

Published online: 13 December 2024

Check for updates

Jiaxin Wang[1,2,3,8], Fangang Meng[4,5,8], Cuiping Xu[6,8], Yanyang Zhang[7], Kun Liang[4], Chunlei Han[4], Yuan Gao[4], Xinguang Yu[7], Zizhou Li[1,2,3], Xiaoyu Zeng[1,2,3], Jun Ni[1,2,3], Huixin Tan[1,2,3], Jiaxin Yang[1,2,3] & Yina Ma[1,2,3,5]

Cooperative interactions profoundly shape individual and collective behaviors of social animals. Successful cooperation requires coordinated efforts by cooperators toward collective goals. However, the underlying behavioral dynamics and neuronal mechanisms within and between cooperating brains remain largely unknown. We recorded intracranial electrophysiological signals from human pairs engaged in a cooperation game. We show that teammate coordination and goal pursuit make distinct contributions to the behavioral cooperation dynamics. Increases and decreases in high-gamma activity in the temporoparietal junction (TPJ) and amygdala distinguish between establishing and maintaining cooperation and forecast transitions between these two states. High-gamma activity from distinct neuronal populations encodes teammate coordination and goal pursuit motives, with populations of TPJ neurons preferentially tracking dominant motives of different cooperation states. Across cooperating brains, high-gamma activity in the TPJ and amygdala synchronizes in a state-dependent manner that predicts how well cooperators coordinate. These findings provide fine-grained understandings of human cooperation dynamics as a state-dependent process with distinctive neurocognitive profiles of each state.

Social animals, including humans, need to establish and maintain cooperative relationships with conspecifics to survive and thrive in an ever-changing environment[1,2]. Successful cooperation relies on concerted efforts by cooperators to achieve collective goals[3–5]. Cooperating parties must not only be motivated to constantly monitor each other's intentions and behaviors for synergistic actions (that is, interpersonal coordination[6,7]) but also strive toward a collective goal (that is, collective goal pursuit[8,9]). Ultimately, efficient cooperation is grounded in the dynamic interplay between these two critical elements[10,11]. Despite the long-standing recognition that cooperation is the continuous and common endeavor of two or more persons to perform a task or reach a goal[4], surprisingly little is known about the behavioral and neuronal mechanisms underlying cooperation dynamics (the dynamic facet of cooperation) and how cooperators (particularly their brains) interact to facilitate cooperation (the multiperson interactive facet of cooperation). Moreover, comprehensive investigations into distinct

[1]State Key Laboratory of Cognitive Neuroscience and Learning, Beijing Normal University, Beijing, China. [2]IDG/McGovern Institute for Brain Research, Beijing Normal University, Beijing, China. [3]Beijing Key Laboratory of Brain Imaging and Connectomics, Beijing Normal University, Beijing, China. [4]Beijing Tiantan Hospital, Capital Medical University, Beijing, China. [5]Chinese Institute for Brain Research, Beijing, China. [6]Department of Functional Neurosurgery, Xuanwu Hospital, Capital Medical University, Beijing, China. [7]Department of Neurosurgery, Chinese PLA General Hospital, Beijing, China. [8]These authors contributed equally: Jiaxin Wang, Fangang Meng, Cuiping Xu. e-mail: yma@bnu.edu.cn

mechanisms governing coordination among cooperators and pursuit of collective goals, as well as their respective contributions to cooperation, are still lacking.

Previous studies have mainly used economic decision-making paradigms (for example, the prisoner's dilemma and coordination game) to assess cooperation[12,13]. These paradigms often oversimplify cooperation as binary choices between cooperation and defection, which fail to capture the complex dynamics of cooperative interactions in real-time feedback settings[14,15]. As a sophisticated form of social alignment, cooperation entails continuous and intensive interaction among cooperators[16]. To unveil the nuanced social processes underlying cooperation dynamics, we developed a virtual interactive cooperation task that provides moment-by-moment measurement of cooperation behaviors and allows us to disentangle the dynamics of two crucial elements in cooperation (interpersonal coordination and collective goal pursuit) in a real-time cooperation setting. We conducted intracranial electroencephalographic (iEEG) recordings of neuronal population activity with millimeter and millisecond resolutions[17] in pairs of cooperators engaged in this dynamic cooperation game (participant and electrode information in Supplementary Table 1; participant dyad information in Supplementary Table 2; experimental setup in Fig. 1a). Combining the dynamic cooperation task and hyper-iEEG recording allows us to unravel (1) how the individual brain tracks the dynamic changes of interpersonal coordination and collective goal pursuit during cooperation process; (2) how neural activities across cooperating minds dynamically synchronize and related to cooperation behaviors; and (3) whether different cooperation states show modulation on intrabrain and interbrain neural patterns.

Drawing insights from research on interpersonal and interagency relationships[18,19] and group dynamics[20], as well as the predictive coding framework of social alignment[21], we propose that interpersonal coordination and collective goal pursuit have predominant roles at different stages of cooperation. During the initiation stage of cooperation, prediction errors inevitably arise because of misalignment of thoughts and movements between cooperators. To establish coordination effectively and prevent its breakdown, cooperators need to accurately perceive and predict socially salient information that undergoes dynamic changes while diligently detecting and rectifying discrepancies between each other. Therefore, prioritizing interpersonal coordination over collective goal pursuit is necessary in response to cooperators' misalignment. However, as cooperation progresses into the maintenance stage, cooperators develop shared representations of movements, thoughts and emotions while also experiencing higher levels of cognitive synchrony through mentalizing and perspective-taking[22,23]. The established alignment between cooperators helps to minimize misalignment[24,25], reduces their focus on interpersonal coordination and increases their synchronized commitment to achieving the collective goal.

Our investigation at the neural level is centered on the amygdala and temporoparietal junction (TPJ) (Fig. 1b), two key regions implicated in cooperative social behaviors, particularly involved in detecting misalignment and facilitating alignment. The amygdala has been found to detect personal space boundaries and maintain an appropriate preference of interpersonal distance[26]. Previous research has also documented the crucial role of the amygdala in detecting and encoding error signals[27] and self–other allocation discrepancy[28]. Furthermore, numerous studies on both humans and nonhumans have evidenced the involvement of the amygdala in social perception[29,30] and in integrating and encoding socially relevant information, particularly that with high social saliency[31,32]. Given that cooperation requires accurate perception of socially salient information and monitoring of self–other misalignment, we propose the amygdala as a prominent candidate participating in cooperative interaction, especially during the initiation stage. The TPJ is an integral part of the mentalizing network and consistently activated during social engagement in various scenarios such as theory-of-mind tasks[33,34], turn-based strategic decision-making[35–37] and face-to-face communications[38]. Specifically, the TPJ has been shown to process social cues[39], infer about others' thoughts or beliefs[40] and preempt others' decisions[41]. Therefore, the recruitment of TPJ during cooperation is expected as cooperators need to track others' behavioral dynamics, understand their intentions and mental states and respond accordingly to achieve coordination. Moreover, simultaneous recordings from multiple human brains using noninvasive techniques such as functional near-infrared spectroscopy, functional magnetic resonance imaging (MRI) and scalp EEG have revealed that correlated neural activity in the TPJ and prefrontal cortex across multiple brains (that is, interbrain neural correlation) engaged in various social interactions[42]. The synchronized neural activity was evident not only during movement coordination[43] but more importantly when achieving higher-level social alignment, including speaker–listener communication[44], parent–child interaction[45], interpersonal cooperation[46] and collective decision-making[47–49]. Recent animal studies also provided valuable evidence of correlated activity of individual neurons and neuronal populations in pairs of interacting mice[50] and bats[51,52], suggesting interbrain correlation as a prominent neural feature of natural social interactions.

However, notable gaps remain in our understanding of whether and how the brains of two individuals interact and coordinate during cooperation. First, human studies have relied on noninvasive techniques that lack the temporal and spatial resolutions required to resolve neuronal population activity[53] and cannot measure neural activity in the high-gamma band. We are particularly interested in investigating the interbrain correlations of high-gamma activity, which have been shown to have a crucial role in social interaction according to animal studies[50–52]. Second, animal research has primarily focused on the frontal cortex[50–52], leaving unknown whether neuronal population activity in other regions crucial for cooperation (for example, TPJ and amygdala) is correlated across cooperating brains. We are particularly interested in investigating interbrain correlations in the amygdala, a deep brain structure. Although the intrabrain evidence has suggested an important role of the amygdala in social cooperation, no prior research has examined whether and how amygdala activity between two individuals is correlated during social interactions. This is challenging because of its deep location and the noninvasive techniques used in previous human studies. By leveraging the strength of iEEG recordings, we can measure neural dynamics at high-frequency bands with fine temporal resolution and specific regions of interest, especially subcortical structures[17].

The three-legged racing game to capture cooperation dynamics

To investigate the dynamics of how cooperating pairs coordinate to achieve a collective goal, we developed a virtual dynamic cooperation task—a computerized three-legged racing game (Fig. 1c,d and Methods). Participants use a computer mouse to maneuver an avatar on a computer screen that is segmented into preparation and racing zones (Fig. 1c). Teammates need to move their avatars toward each other to initiate a connection (a red line visually connects them when their distance is within a preset safe distance) and maintain this connection through the racing zone to the finish line. To simulate challenges of the three-legged race, where teammates may stumble and need to start over, we implemented reset events (definition of key terms in Supplementary Table 3). If the avatars exceed the safe distance in the racing zone, their connection is terminated and they are reset to the preparation zone (henceforth, reset) to re-establish their connection (2.6 ± 4.8 reset events per trial; Fig. 1d; visual demonstration of a single task trial in Supplementary Video 1). This experimental setup provides a naturalistic environment for collecting rich and continuous behavioral data, allowing us to observe genuine cooperation dynamics.

https://doi.org/10.1038/s41593-024-01824-y

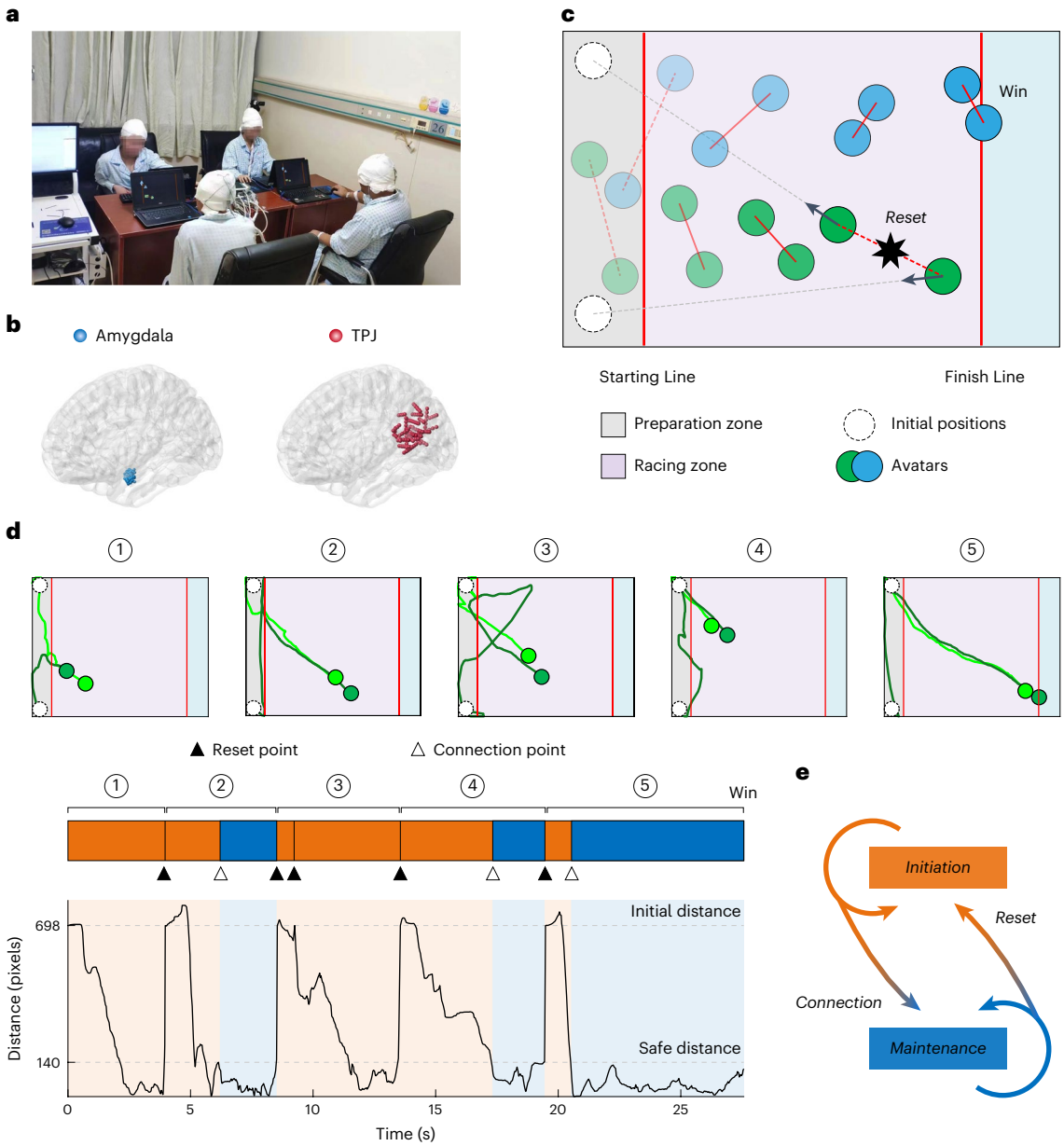

Fig. 1 | Experimental protocol. a, Experimental setup. Shown here is a snapshot of two groups of participants engaging in the three-legged racing game. **b**, The localization of iEEG electrodes in the amygdala and TPJ mapped onto a semitransparent normalized MNI brain (channels located in the right hemisphere are mirrored at their symmetric locations in the left hemisphere). Each colored sphere represents a single channel. The anatomical localization of each channel site was determined and visually inspected within the native space of each participant. **c**, A schematic representation of the virtual three-legged racing game. We use a dashed red line to illustrate a reset event and an 'explosion' symbol to indicate a broken connection; these elements were not present in actual gameplay. **d**, Movement trajectories of a cooperating dyad in an example trial of the three-legged racing game (demonstration of one task trial in Supplementary Video 1). **e**, Two cooperation states. During the trial, a team started in the cooperation initiation state and could progress to maintenance state upon establishing and maintaining a connection for over 2 s. However, if their distance exceeded 140 pixels in the racing zone, they transitioned back to the initiation state through a reset event.

Two cooperation states: initiation and maintenance

We defined two consecutive states in the dynamic cooperation task: initiation of cooperation and maintenance of cooperation (Fig. 1e). When teammates remain connected (their avatars' distance ≤ safe distance) for a duration of 2 s or longer, they are in the state of cooperation maintenance; otherwise, they are in the state of cooperation initiation (that is, time periods when teammates are not connected or connected for less than 2 s). We established the time criterion of 2 s on the basis of its impact on trial success, which was verified by logistic regression analyses (Supplementary Note 1 and Extended Data Fig. 1a,b). In subsequent analyses that focused on temporal profiles of behavioral and neural responses, we performed analyses on the initiation and maintenance epochs defined as the first 2 s in each state. Participant dyads spent a comparable amount of time in both the initiation (47.1%) and the maintenance (52.9%) states, with multiple between-state transitions (Fig. 1d). Participant and healthy dyads showed similar task performance when they played against each other in the same game session (number of win trials between healthy and participant dyads: $t_{12} = -0.862$, $P = 0.4056$, Cohen's $d = -0.445$, 95% confidence interval

(CI): −3.256, 1.410, paired *t*-test; win trial ratios: $\chi^2(1) = 1.862$, $P = 0.172$, χ^2 test). Additionally, both groups exhibited similar state-dependent behavioral patterns in the task (Supplementary Table 4).

To distinguish movement patterns corresponding to the putative main processes (interpersonal coordination and collective goal pursuit) we projected each participant's velocity onto two directions and averaged across teammates (1) the velocity projected onto the position of team center to index interpersonal coordination (v_C; Fig. 2a) and (2) the velocity projected onto the finish line to index collective movement toward the goal (v_G; Fig. 2b). In addition to v_C and v_G, we examined how well teammates synchronized their movement by calculating v_C (v_G) differences between teammates to indicate behavioral cofluctuation. We assessed the impact of behavioral variables on trial success by building trial-level logistic regression models and showed that the percentage of time spent in the maintenance or initiation state yielded a strong influence on trial outcome. v_C, v_G and teammates' v_G difference also contributed to trial outcome (Extended Data Fig. 1c), suggesting that successful cooperation relied on both individual teammate behavior and teammate synchrony.

v_C and v_G captured cooperation dynamics

Participants primarily moved toward teammates in the initiation state ($v_C > v_G$: $t_{24} = 7.676$, $P = 6.515 \times 10^{-8}$, Cohen's $d = 1.953$, 95% CI: 0.708, 1.229, paired *t*-test) and toward the finish line in the maintenance state ($v_C < v_G$: $t_{24} = -16.768$, $P = 9.373 \times 10^{-15}$, Cohen's $d = 4.419$, 95% CI: −2.012, −1.571). A significant velocity × state interaction (Fig. 2c) confirmed distinct contributions of interpersonal coordination and collective goal pursuit to different cooperation states. Additionally, we found that v_C differences were smaller in the maintenance than initiation state (Extended Data Fig. 2), suggesting that cooperation maintenance requires not only moving toward teammates but also achieving better behavioral synchrony in movements. A series of control analyses ensured the robustness of our findings (Supplementary Note 2), including (1) orthogonalizing v_C and v_G directions (Extended Data Fig. 3a,b); (2) using a different interpolation method to ensure smoothness of velocity data (Extended Data Fig. 3c,d); (3) controlling for the opponent's percentage of maintenance state (Supplementary Table 5a); and (4) controlling for dyad demographic information (Supplementary Table 5b). In addition, participants did not show a significant improvement in task performance over time (Supplementary Table 5c).

Next, we analyzed the dynamic changes in v_C and v_G as cooperation progressed by comparing v_C and v_G for each time point in cooperation initiation and maintenance states, respectively. In the initiation state, participants primarily focused on interpersonal coordination, with v_G generally lower than v_C, especially in the 170–1,170-ms time window (cluster-level-corrected *P* value: $P_{corr} < 0.05$; Fig. 2d). However, in the maintenance state, v_G was significantly larger than v_C from 210 ms after onset, with v_G increasing and stabilizing at a high level and v_C decreasing and hovering around zero ($P_{corr} < 0.05$; Fig. 2e). This suggested that teammates quickly adjusted their dominant movement from v_C to v_G in an early time window (from onset to 150 ms) and subsequently moved together toward the finish line at a relatively stable speed.

As the cooperation process frequently alternates between two cooperation states, we assessed behavioral attributes that caused such transitions. During the last 500-ms time window before maintenance-to-initiation transitions (relative to other nontransition maintenance periods), we observed significant v_C decreases and significant v_G increases occurring from 500 ms before reset points ($P_{corr} < 0.05$; v_C in Fig. 2f,g and v_G in Fig. 2h, i). This suggests that poor interpersonal coordination and hasty pursuit of collective goal may jeopardize stable cooperation. Moreover, analysis of the initiation-to-maintenance transitions (versus initiation periods without subsequent transitions) revealed significant v_C increases (Fig. 2j), covering the entire 500 ms before connection points ($P_{corr} < 0.05$; Fig. 2k), without significant changes in v_G (Fig. 2l,m), suggesting that increased interpersonal coordination facilitates well-maintained cooperation.

High-frequency activity distinguished cooperation states

At the neural level, we first investigated neural response patterns during cooperation initiation and maintenance states. Using complex wavelet transform for time–frequency analysis[54], we separately extracted power spectrotemporal maps for each cooperation state. We found significant differences in high-frequency activity between initiation and maintenance states, covering a frequency range of 30–150 Hz (Fig. 3a,b). This power difference was further confirmed by significant power increases in the initiation state but significant decreases in the maintenance state (30–150 Hz; Fig. 3a,b). We individually analyzed state-related high-frequency power (30–150 Hz) for each task session and observed consistent effects across sessions (amygdala, 100%; TPJ, 87%). Furthermore, statistical tests confirmed the robustness of state-dependent high-frequency activity across sessions in both the amygdala ($t_{34} = 11.396$, $P = 3.709 \times 10^{-13}$, Cohen's $d = 3.034$, 95% CI: 0.083, 0.119, paired *t*-test; Fig. 3c) and the TPJ ($t_{29} = 6.296$, $P = 7.086 \times 10^{-7}$, Cohen's $d = 1.280$, 95% CI: 0.031, 0.061; Fig. 3d). Specifically, we found significant power increases in the initiation state (amygdala: $t_{34} = 4.347$, $P = 1.184 \times 10^{-4}$, Cohen's $d = 0.718$, 95% CI: 0.014, 0.039; TPJ: $t_{29} = 2.610$, $P = 0.014$, Cohen's $d = 0.464$, 95% CI: 0.004, 0.034; one-sample *t*-tests) but power decreases in the maintenance state (amygdala: $t_{34} = -15.488$, $P = 5.715 \times 10^{-17}$, Cohen's $d = 2.560$, 95% CI: −0.084, −0.065; TPJ: $t_{29} = -5.081$, $P = 2.024 \times 10^{-5}$, Cohen's $d = 0.903$, 95% CI: −0.038, −0.016).

We further investigated whether the effects observed in the high-frequency band were temporally localized or sustained and identified opposite patterns of significant clusters in initiation and maintenance states in the amygdala and TPJ ($P_{corr} < 0.05$, 10,000 permutations). The initiation state exhibited increased power, covering broad gamma and high-gamma bands, in both the amygdala (significant clusters emerged at initiation onset and lasted up to 1,290 ms, 30–150 Hz; Fig. 3e) and TPJ (one significant cluster between onset and 1,170 ms, 32–150 Hz; another between 1,380 and 2,000 ms, 44–123 Hz; Fig. 3f). The maintenance state featured significant power decreases across a broad frequency range of 30–150 Hz (amygdala, beginning 110 ms after the *maintenance* onset, Fig. 3g; TPJ, from 450 ms after the maintenance onset, Fig. 3h). Direct comparisons of high-frequency power between the initiation and maintenance states revealed significant

Fig. 2 | Behavioral dynamics of team coordination and collective goal pursuit during cooperation. a,**b**, Left, Quantification of team coordination (**a**; v_C, averaged across v_{C1} and v_{C2}) and collective goal pursuit (**b**; v_G, averaged across v_{G1} and v_{G2}) by projecting avatars' velocity onto team center and finish line, respectively. Right, v_C (**a**) measures the average rate of change in distance between the avatar and team center while v_G (**b**) measures the average rate of change in the horizontal distance between the avatar and finish line. **c**, v_C and v_G dominated the initiation and maintenance states, respectively ($F_{1,24} = 283.784$, $P = 8.455 \times 10^{-15}$, $\eta_p^2 = 0.922$, 90% CI: 0.856, 0.945, repeated-measures ANOVA). **d**,**e**, Temporal profiles of v_C and v_G and their contrast across 2-s initiation (**d**) and maintenance (**e**) epochs, respectively. **f**–**i**, Decreasing v_C (**f**,**g**; $t_{24} = -20.327$, $P = 1.239 \times 10^{-16}$, Cohen's $d = 3.937$, 95% CI: −1.027, −0.838) and increasing v_G (**h**,**i**; $t_{24} = 6.609$, $P = 7.778 \times 10^{-7}$, Cohen's $d = 1.280$, 95% CI: 0.644, 1.229) accounted for maintenance-to-initiation transitions. **j**–**m**, Increasing v_C (**j**,**k**; $t_{24} = 9.425$, $P = 1.542 \times 10^{-9}$, Cohen's $d = 1.825$, 95% CI: 1.185, 1.849) with unchanged v_G (**l**,**m**; $P = 0.221$) contributed to initiation-to-maintenance transitions. Data are the mean ± 95% CI. Overlaid dots represent session dyads ($n = 25$). Shaded areas indicate the 95% CI. For visualization of behavioral temporal profiles, time series were smoothed with a 200-ms moving average window, with horizontal lines indicating significant temporal clusters in two-sided permutation tests corrected for multiple comparisons at the cluster level ($P_{corr} < 0.05$, $n = 10{,}000$). Two-sided paired *t*-tests were used in **f**,**j**,**h**,**l**. ***$P < 0.001$; NS, not significant.

https://doi.org/10.1038/s41593-024-01824-y

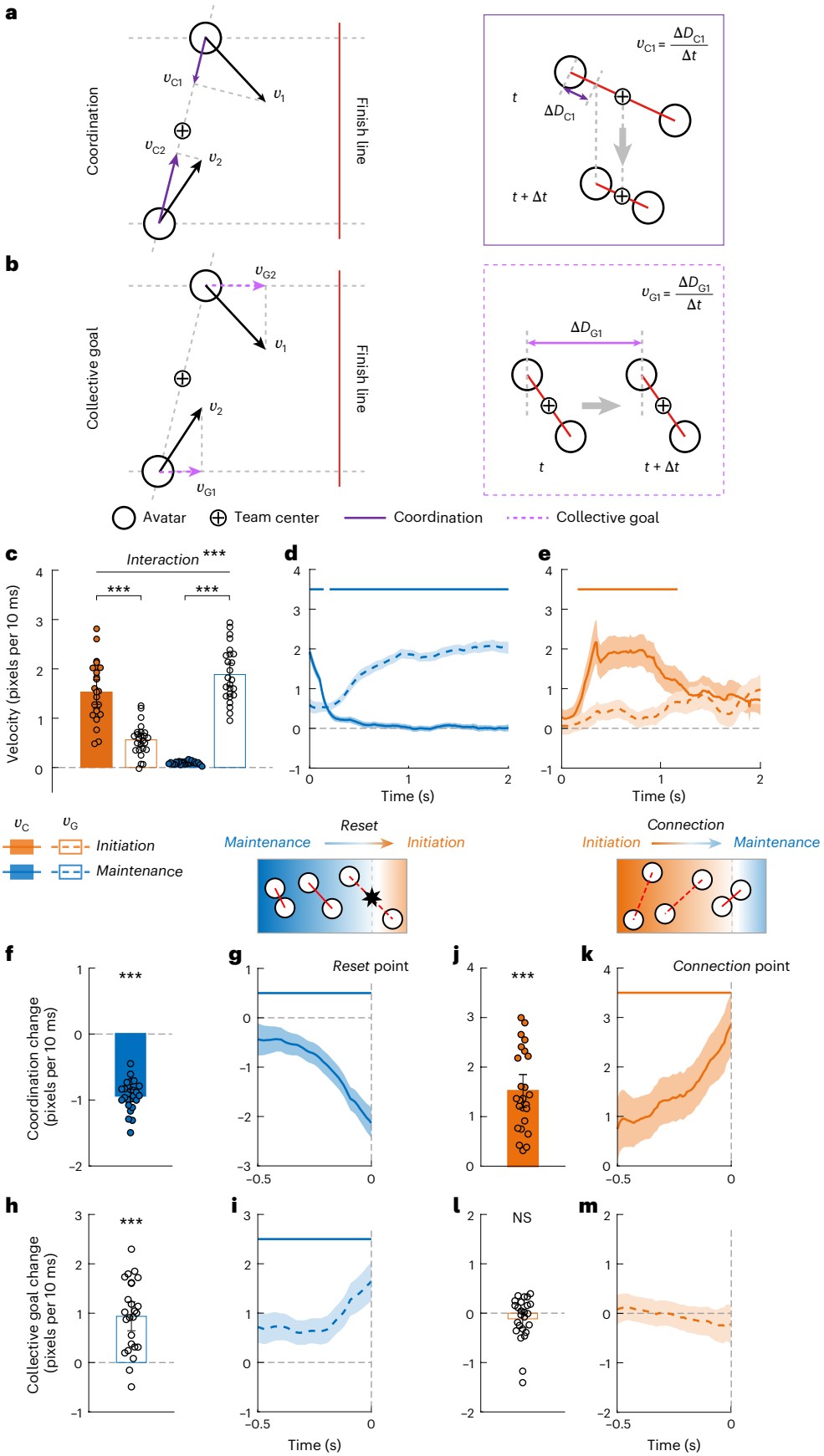

https://doi.org/10.1038/s41593-024-01824-y

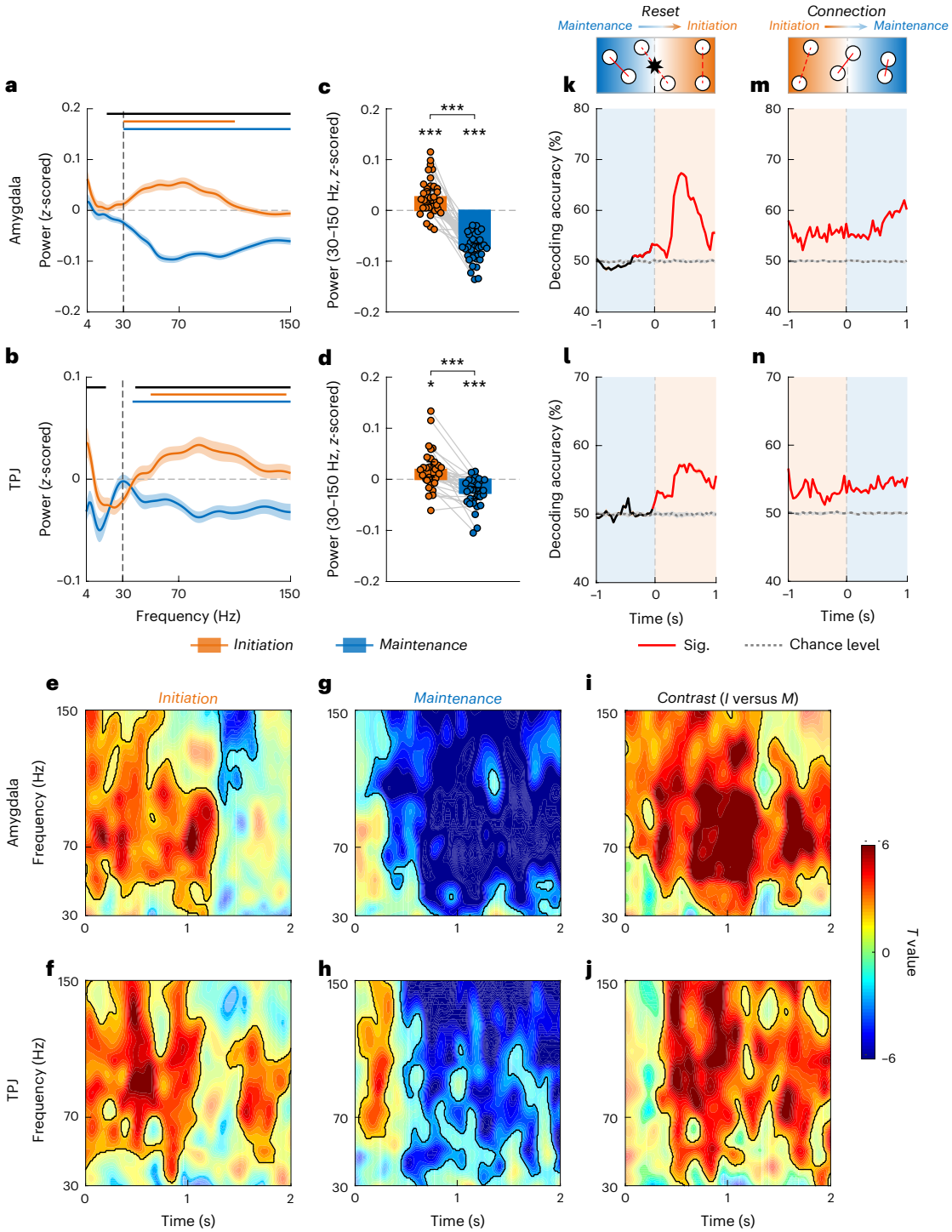

Fig. 3 | State-dependent encoding of cooperation dynamics by high-frequency activity. a,**b**, Normalized amygdala (**a**; $n = 169$ channels) and TPJ (**b**; $n = 258$ channels) activity during cooperation initiation and maintenance states plotted as a function of frequency. Orange and blue curves indicate mean across channels for the initiation state and maintenance state; shaded areas indicate the 95% CI. Horizontal black lines indicate significant frequencies for between-state contrast; horizontal orange and blue lines indicate significant frequencies within 30–150 Hz for each state. **c**,**d**, Significant differences in high-frequency power (30–150 Hz) between initiation and maintenance states in the amygdala (**c**; $t_{34} = 11.396$, $P = 3.709 \times 10^{-13}$, Cohen's $d = 3.034$, 95% CI: 0.083, 0.119, paired t-test) and TPJ (**d**; $t_{29} = 6.296$, $p = 7.086 \times 10^{-7}$, Cohen's $d = 1.280$, 95% CI: 0.031, 0.061, paired t-test). Each dot represents one 'session participant' that was paired in different dyads (amygdala, $n = 35$; TPJ, $n = 30$). Data are the mean ± 95% CI. **e**–**j**, Time–frequency spectrograms (t-value maps) for initiation state (**e**,**f**), maintenance state (**g**,**h**) and between-state contrast (**i**,**j**) in the amygdala and TPJ. For display purposes, power heat maps were smoothed by convolving power time series with a moving Gaussian window of 250 ms for each frequency bin. Black contours delimit significant clusters after two-sided cluster-based permutation tests. **k**–**n**, Amygdala and TPJ high-frequency activity predicted upcoming maintenance-to-initiation (**k**,**l**) and initiation-to-maintenance (**m**,**n**) transitions. SVM classifiers were trained with 90% of the data and tested on the remaining 10%, using a 200-ms time window advanced in 40-ms intervals, with 500 repetitions (Methods). The red and black solid curves indicate time points with significant and insignificant decoding accuracy on test trials, compared to chance-level performance (indicated by gray dotted curves). Significance was determined using one-sided cluster-based permutation tests ($P_{corr} < 0.05$, $n = 10{,}000$). Shaded areas and error bars indicate the 95% CI. Statistical tests were two-sided in **a**–**j**. $^{*}P < 0.05$, $^{**}P < 0.01$ and $^{***}P < 0.001$.

https://doi.org/10.1038/s41593-024-01824-y

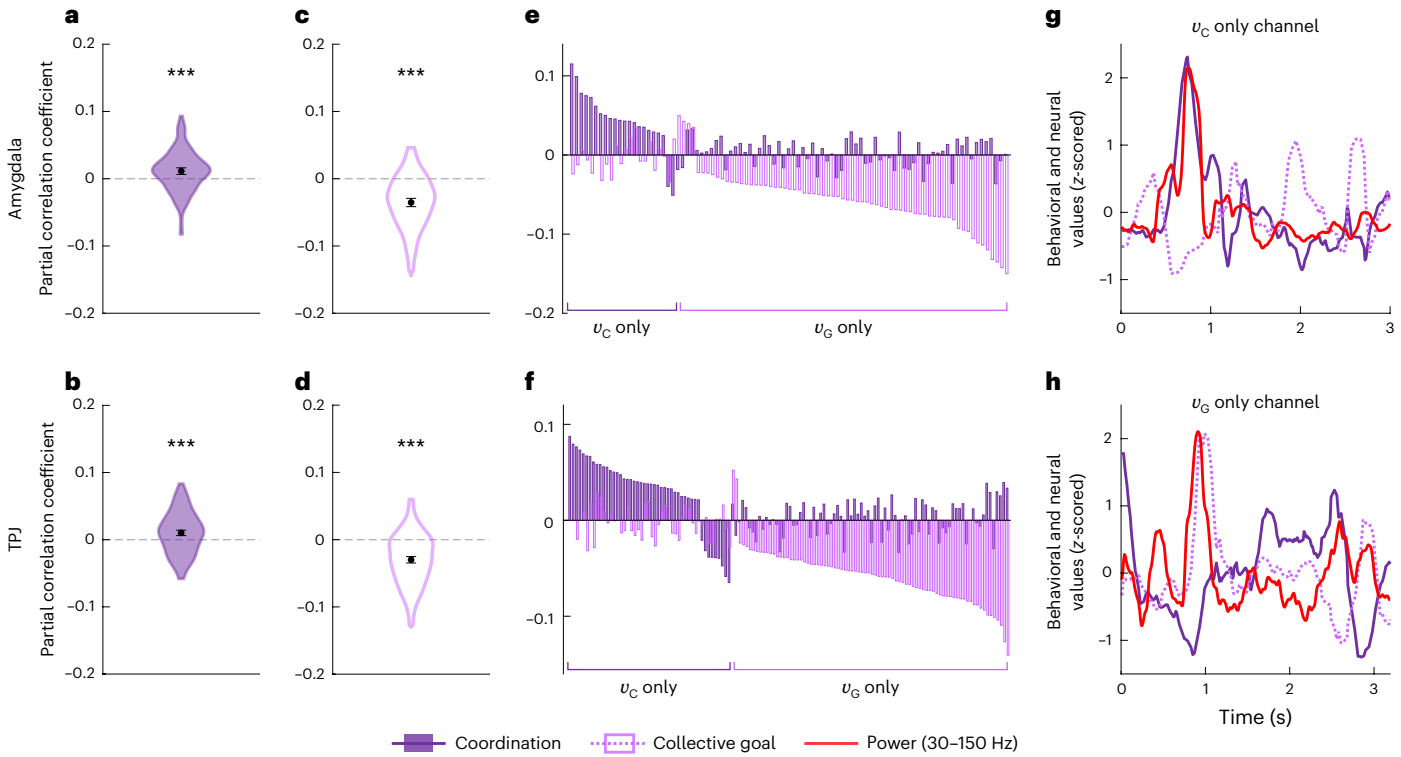

Fig. 4 | Encoding selectivity of neurons to specific cooperation elements. **a**–**d**, High-frequency power (30–150 Hz) positively encoded v_C (**a**, $t_{165} = 4.492$, $P_{FWE} = 2.644 \times 10^{-5}$, Cohen's $d = 0.347$, 95% CI: 0.006, 0.016; **b**, $t_{257} = 4.991$, $P_{FWE} = 2.219 \times 10^{-6}$, Cohen's $d = 0.310$, 95% CI: 0.006, 0.014; one-sample *t*-tests) and negatively encoded v_G (**c**, $t_{168} = -11.311$, $P_{FWE} = 4.105 \times 10^{-22}$, Cohen's $d = 0.866$, 95% CI: −0.042, −0.029; **d**, $t_{256} = -12.293$, $P_{FWE} = 2.645 \times 10^{-27}$, Cohen's $d = 0.765$, 95% CI: −0.035, −0.025; one-sample *t*-tests) across both cooperation states in amygdala ($n = 169$) and TPJ ($n = 258$) channels. **e**,**f**, Encoding coefficients (β, Fisher-transformed) plotted for each channel defined as v_C only and v_G only in the amygdala (**e**) and TPJ (**f**), sorted by the value of the encoding variable in each group. **g**,**h**, Power, v_C and v_G time series for an example v_C only channel in the amygdala (**g**) and an example v_G only channel in the TPJ (**h**) plotted as a function of time in an example trial period. Power, v_C and v_G time series are indicated by red, solid dark purple and dashed light purple lines, respectively. For visualization purposes, behavioral and neural time series were smoothed using a 200-ms moving average window. In **a**–**d**, probability distributions of Fisher-transformed correlation coefficients are shown as violin plots with black dots representing the mean and error bars representing the 95% CI. Outliers of correlation coefficients (mean ± 3 s.d.) were excluded before statistical tests. Statistical tests were two-sided. ***$P < 0.001$, FWE-corrected for multiple comparisons in **a**–**d**.

clusters broadly covering gamma and high-gamma bands (30–150 Hz; Fig. 3i,j). Together, state-dependent cooperation processes were represented by temporally sustained changes in oscillatory power across the high-frequency band in both the amygdala and the TPJ (full frequency spectrograms in Extended Data Fig. 4a–f). Following the common practice in previous hyperscanning studies[47,48], we restricted our frequency of interest (FOI) within the cooperation-related high-frequency band of 30–150 Hz for subsequent intrabrain and interbrain analyses.

High-frequency activity predicted state transitions

We next asked whether and when the high-frequency activity carried sufficient information to detect transitions between cooperation states. Using support vector machine (SVM), we trained classifiers on the 30–150-Hz power to discriminate state transitions from non-transitions (Methods). This analysis was performed within the 2-s time window around each state-transition point (time–frequency maps during state transitions in Extended Data Fig. 4g–j). During maintenance-to-initiation transitions, decoding accuracy significantly exceeded chance levels before reset points (amygdala: 400 ms before reset point, $P_{corr} < 0.05$, Fig. 3k; TPJ: 40 ms before reset point, $P_{corr} < 0.05$, Fig. 3l) and was maintained for 1,000 ms after reset points. An apparent peak accuracy was observed after the reset point in both regions (amygdala: peaking at 440 ms after reset point, 67% accuracy; TPJ: peaking at 560 ms after reset point, 57% accuracy). This suggested that high-frequency activity underwent more dramatic changes around reset points, which may be perceived as a 'surprise' signal. During initiation-to-maintenance transitions, we found early and sustained decoding occurring 1,000 ms before connection points and sustained stability above chance level throughout the whole transition period (±1 s), without a visually evident peak ($P_{corr} < 0.05$; amygdala in Fig. 3m and TPJ in Fig. 3n), suggesting that transitions to cooperation maintenance were characterized by a gradual process, with high-frequency activity exhibiting an early-starting anticipatory effect on when participants established strong connections.

Distinct neuronal populations encoded v_C and v_G dynamics

Considering the distinct roles of v_C and v_G in cooperation, we expected different neural processing of their dynamics. We first investigated whether and how the amygdala and TPJ high-frequency activity tracked moment-by-moment changes in v_C and v_G. We averaged neural activity within the high-frequency band (30–150 Hz) at each time point across the initiation and maintenance states. We entered time series of high-frequency power into a multiple regression analysis performed over all trials that included v_C and v_G time series as parametric regressors, while excluding data during state transitions (±500 ms of each reset or connection event) from the analysis. At the region level (across channels within each brain region), amygdala and TPJ high-frequency activity linearly encoded the v_C and v_G dynamics during cooperation. Increases in high-frequency activity predicted movement toward teammates (Fig. 4a,b), while reductions in high-frequency activity encoded

faster movement toward the finish line (Fig. 4c,d). The encoding of v_C and v_G was not modulated by the anatomical positions within the amygdala and TPJ (correlation between channel site x, y and z coordinates and regression coefficients, all family-wise error-corrected P value (P_{FWE}) > 0.05).

At the neural population level, we asked whether the same or different populations in these regions encoded v_C and v_G. Specifically, we identified encoding channels on the basis of their high-frequency activity that exhibited a significant association with v_C and/or v_G. Channels were considered as v_C only when they significantly tracked v_C but not v_G (and vice versa for v_G only). We found that distinct neuronal populations showed specificity in encoding only v_C (amygdala: 13.0%, Fig. 4e; TPJ: 18.6%, Fig. 4f; example channel in Fig. 4g) or v_G (amygdala: 40.8%, Fig. 4e; TPJ: 31.8%, Fig.4f; example channel in Fig. 4h). Interestingly, a significantly larger number of channels selectively encoded only v_G rather than v_C in both the amygdala ($\chi^2(1) = 23.253$, $P = 1.420 \times 10^{-6}$, McNemar χ^2 test, Yates-corrected) and the TPJ ($\chi^2(1) = 8.377$, $P = 0.004$). Such an encoding preference of v_G was also reflected by a higher predictive strength of v_G (absolute regression coefficients) in channels that encoded both v_C and v_G, especially in the TPJ ($t_{61} = 3.447$, $P = 0.001$, Cohen's $d = 0.463$, 95% CI: 0.005, 0.018, paired t-test).

Next, we asked whether and how these channels encoding v_C and v_G could track finer changes of v_C and v_G within each cooperation state. We conducted the same regression analysis in these channels using neural activity at frequencies that showed significant state-dependent changes (identified in Fig. 3a,b). Interestingly, we found that, in the TPJ, more v_C only channels tracked v_C within the initiation than maintenance state (37.5% versus 8.3%, $\chi^2(1) = 8.450$, $P = 0.004$), while more v_G only channels tracked v_G within the maintenance than initiation state (48.8% versus 22.0%, $\chi^2(1) = 10.5$, $P = 0.001$), suggesting state-dependent encoding of the dominant movement in each state. These findings suggest the functional–anatomic foundations of the cooperation dynamics, highlighting the critical role of populations of TPJ neurons in monitoring real-time changes in state-dependent primary movement throughout the entire cooperation process.

Correlated high-frequency activity across cooperating brains

We tested whether the neural activity of two cooperating individuals was correlated, exhibiting cofluctuations in the time series of high-frequency activity in the amygdala and TPJ and, if so, whether such interbrain correlation depended on the ongoing cooperation states. The relationship between neural activity from teammates was quantified by calculating the Fisher z-transformed Pearson correlation coefficient of their power time series averaged across 30–150 Hz for each same-region channel pair between two cooperating brains. The results revealed that, during both cooperation states, the high-frequency power of cooperating teammates was significantly correlated in both the amygdala (Fig. 5a) and the TPJ (Fig. 5b).

To ensure that the significant interbrain correlation was not because of autocorrelation of neural time series, we tested the statistical significance of the actual interbrain correlation against the null distribution of correlations derived from phase-randomized surrogate time series with identical autocorrelations to those of actual neural time series[50,51]. This analysis revealed that interbrain correlations of high-frequency activity in the amygdala (initiation state, $P < 2 \times 10^{-4}$; maintenance state, $P = 0.003$; Fig. 5c,d) and TPJ (both initiation and maintenance states, $P < 2 \times 10^{-4}$; Fig. 5e,f) were significantly higher than those of phase-randomized signals, further confirming the significantly correlated neural dynamics between cooperating teammates. A similar control analysis was conducted using circularly shifted neural activity to calculate interbrain correlations, which yielded consistent results (Extended Data Fig. 5a–d). Importantly, because cooperation and competition dyads in the same game session shared identical experimental inputs and exhibited comparable motor outputs, the interbrain correlation of competition dyads provides an optimal control condition for that of cooperation dyads. We observed significantly higher interbrain correlations between cooperators than competition dyads in both the amygdala and the TPJ (Extended Data Fig. 5e–h), thus refuting the possibility that correlated neural activity between cooperators was driven by shared environmental inputs and common motor processing.

Moreover, interbrain correlations were dependent on ongoing cooperation states. We observed stronger interbrain correlation of amygdala activity during the initiation than maintenance state ($t_{270} = -4.238$, $P = 3.101 \times 10^{-5}$, Cohen's $d = 0.391$, 95% CI: −0.030, −0.011, paired t-test; Fig. 5a). In contrast, the interbrain correlation of TPJ high-frequency activity was stronger during the maintenance than initiation state ($t_{490} = 3.886$, $P = 1.161 \times 10^{-4}$, Cohen's $d = 0.252$, 95% CI: 0.006, 0.018; Fig. 5b). We further assessed whether such state-dependent interbrain correlations were merely because of real interacting teammates being in the same cooperation state by applying a pseudodyad comparison. To generate pseudodyads, we randomly matched participants who had channels implanted in the same region of interest. This control analysis further confirmed the patterns of state-dependent interbrain correlation in the real interacting dyads (compared to those

Fig. 5 | Significant interbrain correlation between cooperating brains. Significant interbrain correlation at 30–150 Hz between two cooperating brains across all channel pairs in the amygdala (**a**; initiation: $t_{270} = 7.171$, $P = 3.574 \times 10^{-12}$, Cohen's $d = 0.434$, lower 95% CI: 0.021; maintenance: $t_{272} = 2.813$, $P = 0.003$, Cohen's $d = 0.170$, lower 95% CI: 0.003; one-sample t-tests) and TPJ (**b**; initiation: $t_{498} = 5.130$, $P = 2.079 \times 10^{-7}$, Cohen's $d = 0.229$, lower 95% CI: 0.008; maintenance: $t_{494} = 11.776$, $P = 1.100 \times 10^{-28}$, Cohen's $d = 0.528$, lower 95% CI: 0.020, one-sample t-tests). **c**–**f**, Statistical significance of interbrain correlations (in 30–150 Hz) was validated by comparing against null distributions of correlations between phase-randomized surrogate signals. Vertical solid lines indicate observed interbrain correlations in the amygdala (**c**,**d**) and TPJ (**e**,**f**), significantly exceeding the upper limit of 95% CI of the null distributions (dashed lines). **g**,**h**, Significant interbrain correlation after regressing out v_C and v_G from the neural activity of each session participant in amygdala (**g**; initiation: $t_{270} = 6.066$, $P = 2.211 \times 10^{-9}$, Cohen's $d = 0.367$, lower 95% CI: 0.018; maintenance: $t_{272} = 2.699$, $P = 0.004$, Cohen's $d = 0.163$, lower 95% CI: 0.002; one-sample t-tests) and TPJ (**h**; initiation: $t_{497} = 5.094$, $P = 2.489 \times 10^{-7}$, Cohen's $d = 0.228$, lower 95% CI: 0.008; maintenance: $t_{494} = 11.253$, $P = 1.305 \times 10^{-26}$, Cohen's $d = 0.505$, lower 95% CI: 0.019; one-sample t-tests). **i**–**l**, Power correlations plotted as a function of frequency in the amygdala and TPJ for initiation (**i**,**k**) and maintenance (**j**,**l**) states. In **a**–**l**, only positive significant correlation coefficients were considered as valid interbrain synchrony (Methods). In **i**–**l**, the horizontal lines indicate significant positive correlation coefficients obtained from one-sided cluster-based permutation tests, corrected for multiple comparisons at the cluster level ($P_{corr} < 0.05$, $n = 10{,}000$). Shaded areas indicate the lower 95% CI. m,n, Correlation between coordination and the averaged interbrain correlation at 56–89 Hz during the initiation state at amygdala across channel pairs (**m**; $t_{269} = -2.656$, $P_{FWE} = 0.033$, Cohen's $d = 0.161$, 95% CI: −0.025, −0.004, one-sample t-test) and in an example channel pair plotted as a function of time in an example initiation period (**n**; $r = -0.587$, $P = 2.485 \times 10^{-38}$, 95% CI: −0.647, −0.518; behavioral and neural time series were smoothed using a 200-ms moving average window for visualization purposes). **o**, Interbrain correlation at 120–150 Hz negatively correlated with v_C differences during the maintenance state at the TPJ across channel pairs ($t_{497} = -4.028$, $P_{FWE} = 2.608 \times 10^{-4}$, Cohen's $d = 0.180$, 95% CI: −0.017, −0.006, one-sample t-test). **p**, Interbrain correlation at 129–150 Hz negatively correlated with v_G differences during the initiation state at the TPJ across channel pairs ($t_{497} = -4.242$, $P_{FWE} = 1.056 \times 10^{-4}$, Cohen's $d = 0.190$, 95% CI: −0.024, −0.009, one-sample t-test). Probability distributions of Fisher-transformed correlation coefficients for each channel pair (amygdala, $n = 273$; TPJ, $n = 503$) are shown as violin plots with black dots representing the mean and error bars representing the 95% CI. Outliers of correlation coefficients (mean ± 3 s.d.) were excluded before statistical tests. Statistical tests were one-sided in **a**–**l** and two-sided in **m**–**p**. *$P < 0.05$, **$P < 0.01$ and ***$P < 0.001$. In **m**,**o**,**p**, P values were FWE-corrected for multiple comparisons.

https://doi.org/10.1038/s41593-024-01824-y

of pseudodyads), with stronger interbrain correlation during the initiation state in the amygdala and stronger interbrain correlation during the maintenance state in the TPJ (Extended Data Fig. 5i–n). These results validated that state-dependent interbrain correlations only emerged in real cooperating teammates.

We then examined whether the interbrain correlation merely reflected behavioral similarity. Similar to previous studies[51], we regressed out v_C and v_G and recalculated the interbrain correlation between teammate brains. This analysis confirmed (1) significant interbrain correlations in both the amygdala (Fig. 5g) and the TPJ (Fig. 5h) and (2) state-dependent interbrain correlations that were stronger during the initiation than maintenance state in the amygdala ($t_{270} = -3.552$, $P = 4.507 \times 10^{-4}$, Cohen's $d = 0.324$, 95% CI: −0.027, −0.008, paired t-test; Fig. 5g), with an opposite pattern in the TPJ ($t_{489} = 3.427$, $P = 6.623 \times 10^{-4}$, Cohen's $d = 0.220$, 95% CI: 0.004, 0.016; Fig. 5h). These results suggested that interbrain correlation was

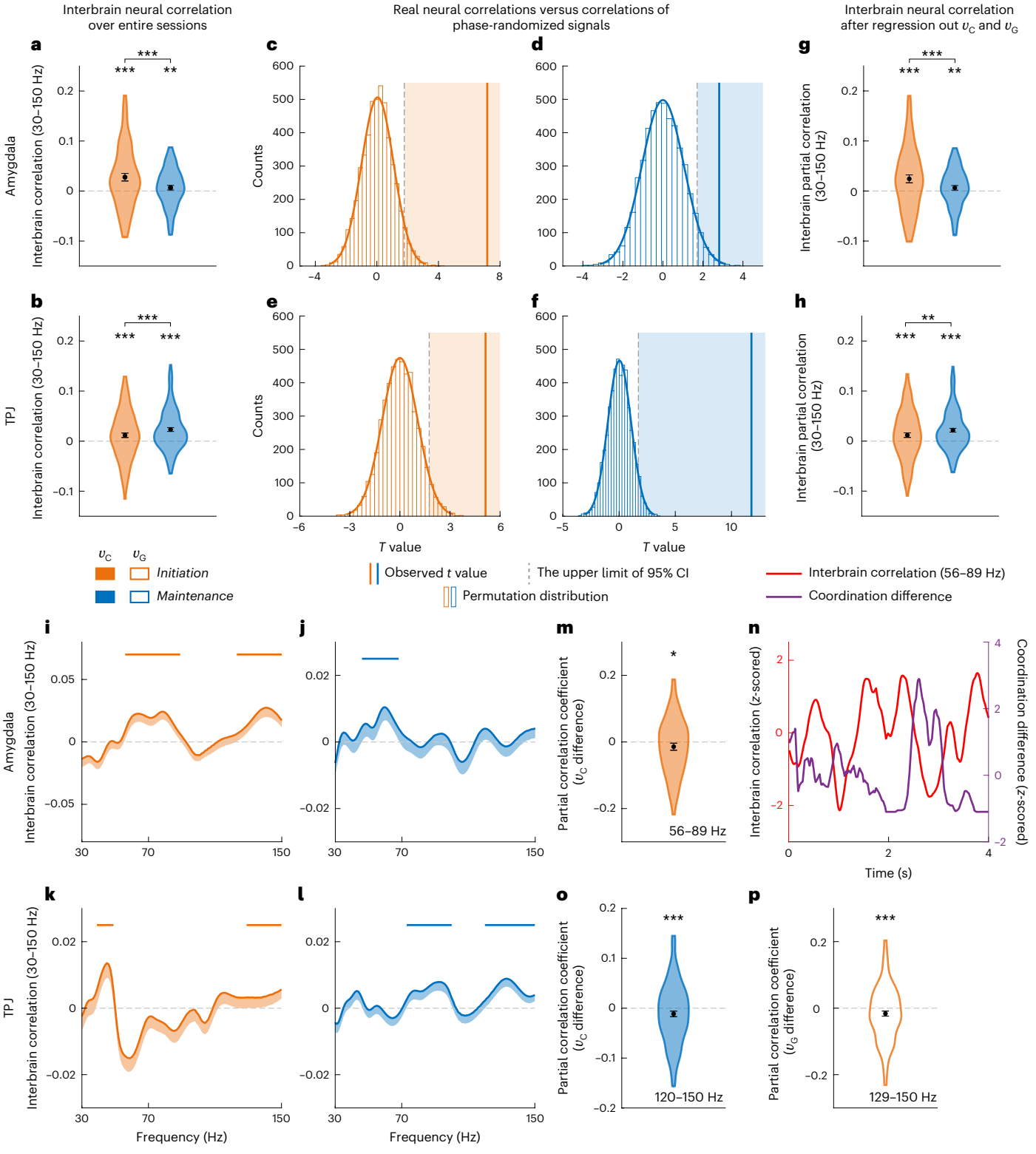

prominent even after controlling for moment-by-moment behavioral adjustments.

Next, we identified the specific spectral profile of interbrain correlations. In the amygdala, significant interbrain correlation was observed at 56–89 Hz and 123–150 Hz during initiation ($P_{corr} < 0.05$; Fig. 5i) and at 46–68 Hz during maintenance ($P_{corr} < 0.05$; Fig. 5j). In the TPJ, significant interbrain correlations were observed during both the initiation (39–49 Hz and 129–150 Hz, $P_{corr} < 0.05$; Fig. 5k) and the maintenance (73–100 Hz and 120–150 Hz, $P_{corr} < 0.05$; Fig. 5l) states. Moreover, we applied a sliding window method to track the temporal profile of interbrain correlation and confirmed opposite patterns of state-dependent interbrain correlations during high-gamma activity (Extended Data Fig. 6). Together, the state-dependent interbrain correlations were reliably observed at both millisecond and second timescales but exhibited region-specific differences with an opposite pattern between the amygdala and the TPJ (control analyses for interbrain correlation in Supplementary Note 3).

Interbrain correlation associated with behavioral dynamics

We concluded our analysis by assessing whether the cofluctuations of neural activities could support teammates' behavioral dynamics. We associated the interbrain correlation with (1) v_C and v_G and (2) behavioral synchrony, represented as differences in v_C and v_G between teammates (Extended Data Fig. 2). We found that amygdala interbrain correlation was associated with synchrony in teammate coordination during the initiation state, indicated by its negative correlation with v_C synchrony (v_C differences between teammates) in the low-gamma band (Fig. 5m,n). This result indicated that more synchronized amygdala activity prompted more similar movement toward teammates when initializing cooperation.

For TPJ, we found that interbrain correlation in the higher-gamma band had a predominate role in encoding cooperation dynamics (full statistical reports in Supplementary Table 6). Specifically, TPJ gamma-band interbrain correlation was negatively correlated with v_G during both the initiation (129–150 Hz, $t_{499} = -2.921$, $P_{FWE} = 0.015$, Cohen's $d = 0.130$, 95% CI: −0.022, −0.004) and maintenance (120–150 Hz, $t_{498} = -2.861$, $P_{FWE} = 0.018$, Cohen's $d = 0.128$, 95% CI: −0.013, −0.002) states. We also found a positive association between TPJ interbrain correlation and v_C during the maintenance state (120–150 Hz, $t_{499} = 3.008$, $P_{FWE} = 0.011$, Cohen's $d = 0.134$, 95% CI: 0.002, 0.008). These results suggested that higher TPJ interbrain correlation suppressed teammates' speed toward the collective goal and facilitated teammate coordination. Moreover, more synchronized gamma-band interbrain correlation in the TPJ facilitated alignment of movements, suggested by negative correlations with the v_C difference during the maintenance state (120–150 Hz; Fig. 5o) and v_G difference during the initiation state (129–150 Hz; Fig. 5p). Additionally, we also found a positive correlation between TPJ interbrain correlation (129–150 Hz) and the v_C difference during the initiation state ($t_{500} = 3.117$, $P_{FWE} = 0.008$, Cohen's $d = 0.139$, 95% CI: 0.005, 0.022). Keeping such v_C differences during the initiation state could potentially establish connection efficiently, as indicated by a positive correlation between larger v_C differences and faster movement toward teammates during initiation ($t_{25} = 14.289$, $P = 3.113 \times 10^{-13}$, Cohen's $d = 2.767$, 95% CI: 0.567, 0.759). Combined, interbrain neural correlation supported interpersonal coordination by increasing the coordination level and diminishing teammate misalignment in coordination in the primary cooperation state that showed higher correlation for each brain region.

Result replication and generalization

We conducted an additional task and analyses to assess the generalizability of our main findings in a noncompetitive context and in teams with more teammates. To this end, we modified the dynamic cooperation task by creating a four-person team in a noncompetitive setting. We designed a noncompetitive cooperative running game with four avatars displayed on the screen, allowing us to control the number of players and adjust the visual complexity between the competitive and noncompetitive conditions. Each four-person team was granted unlimited time to coordinate their avatar movements to cross the finish line while maintaining a safe distance between any two teammate avatars. If distance between any two teammates exceeded the safe distance, all avatars were reset to the preparation zone (Supplementary Video 2).

The main findings from the main dynamic cooperation task were replicated in the noncompetitive settings of the four-person team (Extended Data Figs. 7 and 8). First, at the behavioral level, there was a dissociation of movement for interpersonal coordination and collective goal in two cooperation states. Similarly, v_C dominated the initiation state while v_G dominated the maintenance state. Second, decreased v_C and increased v_G led to maintenance collapses (reset events) whereas increased v_C facilitated cooperation maintenance (long-lasting cooperation). Third, at the neural level, there were significant increases in high-frequency activity (30–150 Hz) in the initiation state but decreases in the maintenance state. Fourth, there was greater behavioral synchrony in the maintenance state. Fifth, significant interbrain correlations were observed in the amygdala during the initiation state and in both states in the TPJ at 30–150 Hz. Last, interbrain correlation also exhibited state dependency, albeit with stronger interbrain correlations in the initiation than maintenance state in both the amygdala and the TPJ. These findings suggested that our main findings were robust regardless of team size (two or four persons) and the type of collective goal (competitive or noncompetitive).

Discussion

While the coordination among cooperators and the pursuit of collective goal are both indispensable[10], it remains unclear whether they operate through distinct mechanisms and how their respective contributions can be differentiated during the course of cooperation. By incorporating an interactive cooperation task and simultaneous recordings of momentary behaviors and iEEG signals from cooperating individuals, we provide a dynamic account of how cognitive and neuronal mechanisms manage the complexity of cooperation. We demonstrate that cooperation is embedded in an iterative structure consisting of two intertwined states, each characterized by a dominant social motive (interpersonal coordination and collective goal pursuit, respectively) and distinctive neural codings (suppressed and enhanced high-frequency neuronal activity) in the amygdala and TPJ. Importantly, we provide compelling evidence of significant state-dependent correlations between neural activity of cooperating individuals, which contribute to their synchronized behaviors, providing a possible neural indicator of cooperation performance. The motive-driven behavioral dynamics, together with the intrabrain and interbrain neural patterns, are suggested to facilitate efficient cooperation because these patterns were more prominent in winning trials than losing trials (Extended Data Fig. 9).

We disentangled interpersonal coordination and collective goal pursuit as two distinct and prominent elements contributing to cooperation in a state-dependent manner, with each element making unique and predominant contributions to different states of cooperation. We argue that interpersonal coordination is a prerequisite for cooperation and the effectiveness of collective goal pursuit is grounded on well-maintained interpersonal coordination, with three supporting lines of evidence. First, efforts toward achieving the collective goal during the initiation state were impeded by a lack of coordination; only through increased coordination was it possible to transition into stable cooperation. Second, effective pursuit of collective goal relies on stabilized interpersonal coordination during the maintenance state. Last, the collapse of cooperation was preceded by more pronounced decreases in interpersonal coordination rather than increases in collective goal pursuit. This suggests that the hasty pursuit of collective

goals was rooted in poor coordination, when cooperators shifted their focus away from each other and blindly concentrated on the collective goal. Together, we provide mechanistic explanations for how the dynamic interplay of interpersonal coordination and collective goal pursuit contributes to cooperation, highlighting the role of coordination as a 'stabilizer' in achieving collective goals. This understanding of interpersonal coordination echoes with the saying 'well begun is half done' and sheds light on how social dilemmas emerge; a lack of interpersonal coordination results in unwillingness to cooperate and prioritization of personal interests, similar to scenarios in the prisoner's dilemma where individuals choose to defect more when communication is not allowed[10,55].

Furthermore, the motives to coordinate with teammates and to pursue the collective goals are disentangled by distinctive neuronal foundations, encoded by high-gamma activity from anatomically dissociated neuronal populations. Moreover, the neural encoding of the crucial cooperation elements was modulated by cooperation states, with subpopulations of TPJ neurons preferentially tracking the moment-by-moment changes of the currently dominant social motive of different cooperation states. We suggest an important role of the TPJ in flexibly identifying and monitoring the primary objectives in the ever-changing social contexts, thereby supporting individuals to make rapid decisions and dynamically adjust their behaviors during complex social interactions[56]. Importantly, we showed that the pursuit of a collective goal is preferably encoded by intraindividual activity with larger encoding neuron populations and greater encoding strength. The negative encoding further indicated the facilitating role of decreased power in pursuing the collective goal. On the other hand, the heightened interbrain neural synchrony had an opposite role by suppressing collective goal pursuit and boosting interpersonal coordination. These results indicate that the distinctive neural mechanisms of intrabrain and interbrain activity patterns were preferentially associated with social motives to pursue the collective goal and to coordinate with teammates, respectively.

The identification of two distinct cooperation states, along with frequent between-state transitions, provides a comprehensive understanding of the complex landscape of cooperative interactions. A crucial question arises as to what triggers these state transitions. Our results indicate that subtle changes in both behavior and neural activity precede the termination of a given state, gradually diverging from its primary characteristics. For example, high-frequency activities in the amygdala and TPJ forecast transitions from the initiation to maintenance state. In parallel, interpersonal coordination surpassed levels observed during the initiation state and exhibited an increasing trend. These findings suggest that deviations in behavioral and neural responses from a current state, coupled with a gradual accumulation of such deviations, serve as reliable precursors for subsequent state transitions.

Animal studies have documented the correlated single-cell spiking and neuronal population activity across brains of socially interacting mice[50] and bats[51,52]. However, obtaining evidence of how interbrain correlation arises from neuronal population activity in humans has been challenging because of the noninvasive nature of neural recording techniques used in previous human studies[53]. Our study addresses this gap by providing direct evidence that high-frequency activity is significantly correlated between two real-time cooperating individuals. Notably, while previous studies have documented interbrain correlations in cortical structures[43–52], we provide initial evidence that the amygdala, a deep brain structure, also exhibits interbrain correlation. Furthermore, our findings extend the understanding of interbrain correlation in humans by highlighting that (1) interbrain correlation is sensitive to social context and more pronounced in high-frequency activity, consistent with previous animal studies[50,51]; (2) interbrain correlation reflects the quality of cooperation by tracking momentary changes in group-level coordination and synchrony between cooperators; and (3) the patterns of interbrain correlation are region specific, with different regions exhibiting varying strengths of interbrain correlations during the same type of social interaction and even opposite patterns when social contexts come into play.

Drawing upon behavioral and neural findings from both individual cooperators and cooperating dyads, we propose a plausible neurocognitive mechanism underlying the dynamic cooperation process that more sociocognitive resources may be required in cooperation initiation relative to maintenance states. At the behavioral level, during cooperation initiation in the current task, teammates need to consistently exert effort to effectively reduce self–other misalignment (that is, distance and differences in movement) and establish a connection, with considerable sociocognitive resources spent on monitoring their teammate's real-time position and encoding their teammate's movement velocity. In contrast, during cooperation maintenance, teammates could stay connected much easier by moving with a similar and relatively constant velocity toward the finish line and maintaining the existing movement patterns. The aligned movements with minimal behavioral variability exempt participants from allocating substantial sociocognitive resources to momentary behavioral adjustment or sophisticated mentalizing during well-maintained cooperation. At the neural level, previous research has documented the crucial roles of the amygdala in detecting and encoding differences between oneself and others[28] and socially relevant information[30], as well as the involvement of the TPJ in mentalizing and perspective-taking[33,34]. Therefore, the heightened amygdala and TPJ high-frequency activity during the initiation state might suggest that greater sociocognitive resources were required to process socially salient information (for example, teammates' position and velocity), perceive self–other differences (that is, differences with and distance from teammate) and engage more intensively in mentalizing processes. Notably, we pointed out that higher behavioral similarity and interbrain synchrony in the TPJ during cooperation maintenance may have a critical role in conserving interacting individuals' sociocognitive resources dedicated to monitoring and mentalizing about each other by minimizing self–other differences and facilitating social alignment[24,57]. This could be linked to reduced TPJ high-frequency activity during cooperation maintenance because we found that higher interbrain correlation was associated with greater decreases in the TPJ activity ($t_{125} = -2.593$, $p = 0.011$, Cohen's $d = 0.230$, 95% CI: −0.001, −0.009, paired t-test). Consistent with our observation, previous work[37] showed that, when faced with successful and satisfactory cooperation decisions, there were reduced TPJ activity and increased interbrain TPJ synchrony between cooperators. Together, this potentially highlights the biological significance of interbrain correlation and represents an adaptive mechanism through which neural systems operate, particularly in complex social interactions. While these lines of evidence support the sociocognitive resource hypothesis, we encourage future studies to empirically test this hypothesis.

To conclude, this study represents a pioneering effort in tracking individual neuronal activity and brain-to-brain coupling in relation to cooperation dynamics, providing a deeper comprehension of the cognitive and neural mechanisms underlying real-time, interactive human cooperation. Our findings remained reliable when extended to noncompetitive, multiple-person cooperation scenarios. The behavioral dynamics also exhibited robustness across healthy controls and participants with epilepsy. We also highlight the promising methodology of using physical variables with multiple dimensions and high temporal resolution as behavioral measurements, which could provide insights into the dynamic processes underlying real-time interactive behaviors in human or animals.

While our experiment entailed a win–win scenario for cooperating parties, it is important to note that social dilemmas, such as the prisoner's dilemma and public goods problems, involve trade-offs between individual and collective interests. Therefore, understanding how people dynamically weigh their own interests against collective ones and

how free-riding behavior emerges in such situations remain important topics for future research. We also bring out potential refinements to the current task design, such as incorporating a dynamic goal or adjusting the parameter of safe distance, which could capture more complex behavioral dynamics during cooperation. Unfortunately, because of the practical constraints of iEEG recordings, our study had limited coverage of implanted electrodes in the brain. Understanding how other brain regions (for example, reward-related and motor-related regions) are involved in the cooperation process remains unresolved for future research. We hope that our experimental paradigm and neural findings inspire future studies using iEEG technology and dynamic experimental designs to investigate whether our findings generalize to other cooperation scenarios and social groups and how other brain regions participate in the cooperation dynamics. Ultimately, addressing these questions could provide practical guidelines for individuals and groups for managing misunderstandings and malfunctions in cooperative situations across society.

Online content

Any methods, additional references, Nature Portfolio reporting summaries, source data, extended data, supplementary information, acknowledgements, peer review information; details of author contributions and competing interests; and statements of data and code availability are available at https://doi.org/10.1038/s41593-024-01824-y.

References

1. Gadagkar, R. *Survival Strategies: Cooperation and Conflict in Animal Societies* (Harvard Univ. Press, 1997).
2. Henrich, N. & Henrich, J. P. *Why Humans Cooperate: A Cultural and Evolutionary Explanation* (Oxford Univ. Press, 2007).
3. Fairchild, H. P. *Dictionary of Sociology* (Philosophical Library, 1944).
4. A. W. Green, *Sociology: An Analysis of Life in Modern Society* (McGraw-Hill, 1972).
5. Merrill, F. E. *Society and Culture: An Introduction to Sociology* (Prentice-Hall, 1965).
6. Bernieri, F. J. & Rosenthal, R. Interpersonal coordination: behavior matching and interactional synchrony. In *Fundamentals of Nonverbal Behavior* (eds Feldman, R. S. & Rimé, B.) (Cambridge Univ. Press, 1991).
7. Sebanz, N., Bekkering, H. & Knoblich, G. Joint action: bodies and minds moving together. *Trends Cogn. Sci.* **10**, 70–76 (2006).
8. Tomasello, M. & Carpenter, M. Shared intentionality. *Dev. Sci.* **10**, 121–125 (2007).
9. Sacheli, L. M., Aglioti, S. M. & Candidi, M. Social cues to joint actions: the role of shared goals. *Front. Psychol.* **6**, 145878 (2015).
10. Agarwal, R., Croson, R. & Mahoney, J. T. The role of incentives and communication in strategic alliances: an experimental investigation. *Strateg. Manag. J.* **31**, 413–437 (2010).
11. Gulati, R., Wohlgezogen, F. & Zhelyazkov, P. The two facets of collaboration: cooperation and coordination in strategic alliances. *Acad. Manag. Ann.* **6**, 531–583 (2012).
12. Sanfey, A. G. Social decision-making: insights from game theory and neuroscience. *Science* **318**, 598–602 (2007).
13. Lee, D. Game theory and neural basis of social decision making. *Nat. Neurosci.* **11**, 404–409 (2008).
14. Yoo, S. B. M., Hayden, B. Y. & Pearson, J. M. Continuous decisions. *Philos. Trans. R. Soc. B Biol. Sci.* **376**, 20190664 (2021).
15. Gordon, J. et al. The road towards understanding embodied decisions. *Neurosci. Biobehav. Rev.* **131**, 722–736 (2021).
16. Gallotti, M., Fairhurst, M. T. & Frith, C. D. Alignment in social interactions. *Conscious. Cogn.* **48**, 253–261 (2017).
17. Parvizi, J. & Kastner, S. Promises and limitations of human intracranial electroencephalography. *Nat. Neurosci.* **21**, 474–483 (2018).
18. Berger, C. R. & Calabrese, R. J. Some explorations in initial interaction and beyond: toward a developmental theory of interpersonal communication. *Hum. Commun. Res.* **1**, 99–112 (1974).
19. Mohr, J. & Spekman, R. Characteristics of partnership success: partnership attributes, communication behavior, and conflict resolution techniques. *Strateg. Manag. J.* **15**, 135–152 (1994).
20. Tuckman, B. W. Developmental sequence in small groups. *Psychol. Bull.* **63**, 384 (1965).
21. Shamay-Tsoory, S. G., Saporta, N., Marton-Alper, I. Z. & Gvirts, H. Z. Herding brains: a core neural mechanism for social alignment. *Trends Cogn. Sci.* **23**, 174–186 (2019).
22. Stolk, A., Verhagen, L. & Toni, I. Conceptual alignment: how brains achieve mutual understanding. *Trends Cogn. Sci.* **20**, 180–191 (2016).
23. Rossignac-Milon, M. & Higgins, E. T. Epistemic companions: shared reality development in close relationships. *Curr. Opin. Psychol.* **23**, 66–71 (2018).
24. Koban, L., Ramamoorthy, A. & Konvalinka, I. Why do we fall into sync with others? Interpersonal synchronization and the brain's optimization principle. *Soc. Neurosci.* **14**, 1–9 (2017).
25. Fotopoulou, A. & Tsakiris, M. Mentalizing homeostasis: the social origins of interoceptive inference. *Neuropsychoanalysis* **19**, 3–28 (2017).
26. Kennedy, D. P., Gläscher, J., Tyszka, J. M. & Adolphs, R. Personal space regulation by the human amygdala. *Nat. Neurosci.* **12**, 1226–1227 (2009).
27. Gottfried, J. A., O'Doherty, J. & Dolan, R. J. Encoding predictive reward value in human amygdala and orbitofrontal cortex. *Science* **301**, 1104–1107 (2003).
28. Liu, Y. et al. Oxytocin modulates social value representations in the amygdala. *Nat. Neurosci.* **22**, 633–641 (2019).
29. Rutishauser, U., Mamelak, A. N. & Adolphs, R. The primate amygdala in social perception—insights from electrophysiological recordings and stimulation. *Trends Cogn. Sci.* **38**, 295–306 (2015).
30. Adolphs, R. What does the amygdala contribute to social cognition? *Ann. N. Y. Acad. Sci.* **1191**, 42–61 (2010).
31. Gothard, K. M., Battaglia, F. P., Erickson, C. A., Spitler, K. M. & Amaral, D. G. Neural responses to facial expression and face identity in the monkey amygdala. *J. Neurophysiol.* **97**, 1671–1683 (2007).
32. Anderson, A. K. & Phelps, E. A. Lesions of the human amygdala impair enhanced perception of emotionally salient events. *Nature* **411**, 305–309 (2001).
33. Aichhorn, M., Perner, J., Kronbichler, M., Staffen, W. & Ladurner, G. Do visual perspective tasks need theory of mind? *Neuroimage* **30**, 1059–1068 (2006).
34. Saxe, R. & Kanwisher, N. People thinking about thinking people: the role of the temporo-parietal junction in 'theory of mind'. *Neuroimage* **19**, 1835–1842 (2003).
35. Bhatt, M. A., Lohrenz, T., Camerer, C. F. & Montague, P. R. Neural signatures of strategic types in a two-person bargaining game. *Proc. Natl Acad. Sci. USA* **107**, 19720–19725 (2010).
36. Morishima, Y., Schunk, D., Bruhin, A., Ruff, C. C. & Fehr, E. Linking brain structure and activation in temporoparietal junction to explain the neurobiology of human altruism. *Neuron* **75**, 73–79 (2012).
37. Tang, H. et al. Interpersonal brain synchronization in the right temporo-parietal junction during face-to-face economic exchange. *Soc. Cogn. Affect. Neurosci.* **11**, 23–32 (2016).
38. Redcay, E. et al. Live face-to-face interaction during fMRI: a new tool for social cognitive neuroscience. *Neuroimage* **50**, 1639–1647 (2010).

39. Walbrin, J., Downing, P. & Koldewyn, K. Neural responses to visually observed social interactions. *Neuropsychologia* **112**, 31–39 (2018).
40. Sommer, M. et al. Neural correlates of true and false belief reasoning. *Neuroimage* **35**, 1378–1384 (2007).
41. Carter, M. C., Bowling, D. L., Reeck, C. & Huettel, S. A. A distinct role of the temporo-parietal junction in predicting socially guided decisions. *Science* **337**, 109–111 (2012).
42. Czeszumski, A. et al. Hyperscanning: a valid method to study neural inter-brain underpinnings of social interaction. *Front. Hum. Neurosci.* **14**, 39 (2020).
43. Cheng, X., Guo, B. & Hu, Y. Distinct neural couplings to shared goal and action coordination in joint action: evidence based on fNIRS hyperscanning. *Soc. Cogn. Affect. Neurosci.* **17**, 956–964 (2022).
44. Jiang, J. et al. Neural synchronization during face-to-face communication. *J. Neurosci.* **32**, 16064–16069 (2012).
45. Piazza, E. A., Hasenfratz, L., Hasson, U. & Lew-Williams, C. Infant and adult brains are coupled to the dynamics of natural communication. *Psychol. Sci.* **31**, 6–17 (2020).
46. Cui, X., Bryant, D. M. & Reiss, A. L. NIRS-based hyperscanning reveals increased interpersonal coherence in superior frontal cortex during cooperation. *Neuroimage* **59**, 2430–2437 (2012).
47. Yang, J., Zhang, H., Ni, J., De Dreu, C. K. W. & Ma, Y. Within-group synchronization in the prefrontal cortex associates with intergroup conflict. *Nat. Neurosci.* **23**, 754–760 (2020).
48. Zhang, H., Yang, J., Ni, J., De Dreu, C. K. W. & Ma, Y.Leader–follower behavioural coordination and neural synchronization during intergroup conflict. *Nat. Hum. Behav.* **7**, 2169–2181 (2023).
49. Ni, J., Yang, J. & Ma, Y. Social bonding in groups of humans selectively increases inter-status information exchange and prefrontal neural synchronization. *PLoS Biol.* **22**, e3002545 (2024).
50. Kingsbury, L. et al. Correlated neural activity and encoding of behavior across brains of socially interacting animals. *Cell* **178**, 429–446 (2019).
51. Zhang, W. & Yartsev, M. M. Correlated neural activity across the brains of socially interacting bats. *Cell* **178**, 413–428 (2019).
52. Rose, M. C., Styr, B., Schmid, T. A., Elie, J. E. & Yartsev, M. M. Cortical representation of group social communication in bats. *Science* **374**, eaba9584 (2021).
53. Sejnowski, T. J., Churchland, P. S. & Movshon, J. A. Putting big data to good use in neuroscience. *Nat. Neurosci.* **17**, 1440–1441 (2014).
54. Oostenveld, R., Fries, P., Maris, E. & Schoffelen, J. M. FieldTrip: open source software for advanced analysis of MEG, EEG, and invasive electrophysiological data. *Comput. Intell. Neurosci.* **2011**, 1–9 (2011).
55. Dawes, R. M., McTavish, J. & Shaklee, H. Behavior, communication, and assumptions about other people's behavior in a commons dilemma situation. *J. Pers. Soc. Psychol.* **35**, 1 (1977).
56. Geng, J. J. & Vossel, S. Re-evaluating the role of TPJ in attentional control: contextual updating? *Neurosci. Biobehav. Rev.* **37**, 2608–2620 (2013).
57. Tamir, D. I. & Mitchell, J. P. Neural correlates of anchoring-and-adjustment during mentalizing. *Proc. Natl Acad. Sci. USA* **107**, 10827–10832 (2010).

Methods

Participants

A total of 31 persons with epilepsy (19 males, age = 25.8 ± 9.2 years old; demographic details in Supplementary Table 1) participated in this study. All participants were implanted with intracranial depth electrodes and underwent iEEG recording to locate the seizure onset zone, with electrode placement determined exclusively on the basis of clinical requirements. All participants recruited for this study had no history of psychiatric disorders, head trauma or encephalitis. Three participants were excluded from neural analysis as they did not have electrodes implanted in the amygdala and TPJ contralateral to or outside of the epileptogenic zone. The final neural dataset consisted of 25 participants (16 males, age = 27.5 ± 9.0 years old).

The experimental protocols were in accordance with the latest version of the Declaration of Helsinki and received approval from the local institutional review board at each hospital (Chinese PLA General Hospital, S202139402; Beijing Xuanwu Hospital, ClinRes No. 2022018; Beijing Tiantan Hospital, KY 202008002). Before participation, all participants provided informed consent and acknowledged their right to withdraw at any time during the study. The experiment involved no deception and participants received compensation for their participation.

In each experimental session, we recruited four participants (four participants with epilepsy or two participants with epilepsy and two healthy controls). Four participants undergoing simultaneous iEEG monitoring were paired into two two-participant teams and played against each other ('PP–PP' session). When only two participants were recorded simultaneously, two healthy participants were paired as a team to play with the participant team ('PP–HH' session). We performed 7 PP–PP sessions and 13 PP–HH sessions involving 25 different dyads of participants with epilepsy (Supplementary Table 2) and 13 dyads of healthy participants. Similar to previous studies[50,51], some participants participated in multiple experimental sessions but were paired in different dyads, thus being considered as distinct 'session participants' for the analysis at the single-individual level. The behavioral and neural analysis reported in the main text was based on participants. Dyads of participants with epilepsy and healthy controls exhibited similar behavioral patterns (Supplementary Table 4).

Sample size estimation

Similar to the majority of iEEG studies[58–64], we did not conduct a prior sample size estimation. For individual-level analyses, numbers of clean channels in regions of interest (amygdala: 169 channels, TPJ: 258 channels; Supplementary Table 1) were similar to or larger than those reported in other iEEG publications[62,63,65,66]. For dyad-level analyses, the numbers of dyads and channel pairs (Supplementary Table 2) were comparable to those reported in animal studies examining interbrain correlation[50,51], as there was no existing hyper-iEEG study conducted on humans. Moreover, our main findings are statistically highly significant and robust across individual participants while surviving multiple-comparison correction.

Experimental procedure and tasks

For each experimental session, a group of four participants (two dyads of participants with epilepsy or one dyad of participants with epilepsy and one healthy dyad) were introduced to each other. They then completed an individual practice session (~2 min) to familiarize with avatar control and experimental settings. Participants then engaged in both the three-legged racing game and the cooperative running game without any form of communication allowed between them throughout these tasks. These tasks were implemented using Psychtoolbox[67] for MATLAB (MathWorks).

Main task: a computerized three-legged racing game. The main task is inspired by real-life three-legged race and adapted into a real-time interactive virtual game where two two-person competing teams aim to outpace their opponent and cross the finish line first.

Each participant uses a computer mouse to control an on-screen colored shape that acts as their avatar, with its position determined by the location of the mouse pointer. The avatars are designed as four distinct polygons in two colors, with teammates sharing the same color. The game field is divided into three zones—preparation zone, racing zone and finish zone—by two vertical red lines (Fig. 1c). At the beginning of each trial, each avatar appears in a preset initial position in the preparation zone. During gameplay, relationships between teammate avatars can be either connected or disconnected on the basis of their distance. If their distance is below a predetermined safe distance of 140 pixels, a red line between teammate avatars indicates that they are connected; otherwise, no line is shown between them to indicate that they are disconnected. These rules interact with different field zones such that (1) avatars can move freely if one or both teammate avatars are in the *preparation* zone; (2) avatars must remain connected to enter and move through the racing zone; (3) if the connection between teammate avatars breaks in the racing zone, both will immediately reset to their initial positions within the preparation zone; and (4) once any one avatar on a team crosses over the finish line before the opponents do so, then this concludes trial with victory for this team (Supplementary Video 1).

Participants were explicitly informed about the competitive nature of the game between teams. To win the game, they had to move toward the finish line as quickly as possible while staying connected with their teammate. Throughout gameplay, all participants viewed identical displays through an intranet connection that provided simultaneous real-time updates on each avatar's position and teammate avatars' relationship. Upon one team crossing the finish line, there was a 1,000-ms screen freeze to clearly visualize each avatar's final position, followed by a jittered fixation for 800 ms (600–1,000 ms). Subsequently, a feedback screen appeared for 2,000 ms indicating the trial outcome, followed by an 800-ms intertrial interval (600–1,000 ms).

Replication task: the cooperative running game. We entered each four-person participant group into a modified cooperation task that involved no competition and more teammates: the cooperative running game (details in Extended Data Fig. 7a). There was only one four-person team, aiming to cross the finish line together without competition. This task was designed to assess the generalizability of the main findings from the three-legged racing game. Although exploring differences between competitive and cooperative contexts is beyond the scope of this study, it is an intriguing question worthy of future investigation.

iEEG recordings

iEEG data acquisition. iEEG data were recorded using amplifiers from the Nicolet EEG system at the Chinese PLA General Hospital, Nihon-Kohden system at Beijing Tiantan Hospital and Micromed system at Xuanwu Hospital, with sampling rates of 4,096, 2,000 and 1,024 Hz, respectively. The online recording signals of all contacts were referenced to a common contact that was simultaneously recorded. Each depth electrode was 0.8 mm in diameter and contained 8–20 contacts (2 mm in length, 1.5 mm apart). iEEG data were collected when no subclinical or clinical seizures occurred during or immediately before the task. It was ensured that medications, including conventional antiseizure medications and GABA-mediating drugs, were restricted for participants several hours before iEEG recordings of our tasks.

Electrode localization. High-resolution postoperative head computed tomography (CT) and preoperative structural MRI scans were obtained for each participant[68]. We aligned the CT and MRI scans to the anterior commissure posterior commissure coordinate system. The location of contacts was identified by reconstructing the MRI and coregistering it with the CT image. The anatomical locations of all channels were determined in each participant's native brain space. For visualization purposes, channel positions were transformed into

the Montreal Neurological Institute (MNI) space and plotted using BrainNet Viewer[69] with a high-resolution 'ICBM152' (International Consortium for Brain Mapping) template brain. All these steps were performed using FieldTrip toolbox[54], Freesurfer software[70] (https://surfer.nmr.mgh.harvard.edu/) and Statistical Parametric Mapping (SPM12)[71] implemented in MATLAB.

Behavioral analyses

On the basis of the participants' movement trajectories, we derived a series of physical indices that represented cooperation dynamics. Main indices included team coordination (v_C), collective goal pursuit (v_G), the difference in v_C and the difference in v_G. According to the presence and duration of teammate connections, we defined two nonoverlapping states during the dynamic cooperation game: cooperation initiation state and cooperation maintenance state (Supplementary Note 1). We first focused on both grand averages and temporal profiles of behavioral indices within and between cooperation states. We then investigated behavioral changes during between-state transitions. Last, we examined how cooperative behaviors contribute to trial outcome (Extended Data Fig. 1c) and conducted behavioral control analyses (Supplementary Note 2).

Behavioral movement decomposition. We resorted to Newtonian variables to physically quantify real-time movement. Motor-related variables (for example, velocity) could provide insights into participants' internal states and motives in real time[72–74]. We extracted each avatar's position from each time point to define a time series of x and y coordinates (in pixels, originally sampled at ~20 Hz). We then interpolated the position data to 100 Hz using linear methods. For an avatar, the instantaneous velocity at time t (a vector, with both magnitude and direction) was defined as follows:

$$\boldsymbol{v}(t) = \frac{\boldsymbol{P}(t) - \boldsymbol{P}(t - \Delta t)}{\Delta t}$$

where $\boldsymbol{P}(t)$ indicates the position vector of the avatar at time t, and Δt is the sampling interval (10 ms).

To quantify movement for interpersonal coordination and collective goal pursuit, we projected each teammate avatar's velocity vector onto a unit vector pointing toward the team center or finish line and averaged across teammates as a dyad-level index:

$$v_C(t) = \frac{1}{2}(\boldsymbol{v}_1 \cdot \boldsymbol{n}_1^c + \boldsymbol{v}_2 \cdot \boldsymbol{n}_2^c)$$

$$v_G(t) = \frac{1}{2}(\boldsymbol{v}_1 \cdot \boldsymbol{n}_x + \boldsymbol{v}_2 \cdot \boldsymbol{n}_x)$$

where $\boldsymbol{v}_1$ and $\boldsymbol{v}_2$ are velocities of avatars in a dyad, $\boldsymbol{n}_i^c$ denotes a unit vector with length equal to one that points from avatar i's position to the center of the team ($i = 1$ or 2; in this case, $\boldsymbol{n}_1^c = -\boldsymbol{n}_2^c$) and $\boldsymbol{n}_x$ denotes the unit vector indicating the direction to the finish line. Note that v_C measures how fast teammate avatars approach the team center ($v_C(t) = (\Delta D_{C1} + \Delta D_{C2})/2\Delta t$, where D_C is the distance between the avatar and the team center), whereas v_G measures how fast the team (represented by the center) approaches the finish line ($v_G(t) = (\Delta D_{G1} + \Delta D_{G2})/2\Delta t$, where D_G denotes the horizontal distance between the avatar and the finish line).

We measure behavioral similarity by calculating absolute value differences in v_C and v_G between teammate avatars: $|\boldsymbol{v}_1 \cdot \boldsymbol{n}_1^c - \boldsymbol{v}_2 \cdot \boldsymbol{n}_2^c|$ for coordination difference and $|\boldsymbol{v}_1 \cdot \boldsymbol{n}_x - \boldsymbol{v}_2 \cdot \boldsymbol{n}_x|$ for collective goal pursuit difference.

We performed several quality checks on the behavioral data to eliminate noises and extreme values in our following analysis: (1) replacing time points with a velocity magnitude above the 99th quantile across all sessions with null values; (2) removing data within a 1-s time window around reset points to minimize the impact of unstable movements during reset events when we analyzed profiles of the initiation state rather than the transition time window; and (3) removing data within the 1-s time window around between-state transitions when we performed the behavioral–neural correlation analysis.

Cooperation states. We observed that teammate avatars frequently showed transient connections. To attenuate noises caused by these short-lived connections while identifying an appropriate duration for a connected period that can effectively contribute to game victory, we applied trial-level logistic mixed-effect model analysis to define a less-connected initiation state and a well-connected maintenance state (Supplementary Note 1). The maintenance state refers to time periods when avatars remained connected for at least 2 s and the initiation state refers to time periods apart from maintenance states. To ensure accurate assessment of temporal information of behavioral or neural profiles, our analysis was restricted to initiation and maintenance epochs, which refer to the first 2 s of initiation and maintenance periods, respectively. We did not include initiation periods lasting less than 2 s when conducting temporal analysis. This allowed us to compare the temporal profile of two cooperation states using the same timescale of 2 s.

To investigate the behavioral profile during each cooperation state, we averaged v_C and v_G values, as well as differences in v_C and v_G, across all time points separately in cooperation initiation and maintenance states for each dyad. We conducted a dyad-level repeated-measures analysis of variance (ANOVA) on v_C and v_G using state and velocity as two within-dyad variables. Paired t-tests were performed to determine significant differences in behavioral synchrony between states at the dyad level. To further reveal the temporal profile of v_C and v_G in each state, we aggregated the 2-s initiation and maintenance epochs across all participants. Nonparametric cluster-based permutation was used to compare v_C and v_G values, as well as differences in v_C and v_G, at each time point across all epochs for each cooperation state to identify temporal clusters with significant differences between v_C and v_G. The numbers of initiation and maintenance epochs were balanced by randomly selecting a subset of epochs with more occurrences to match the number of epochs with fewer occurrences for each dyad in Extended Data Fig. 2b,d. To visualize the temporal profile of behavioral indices, we smoothed the behavior data time series using a moving average window of 200 ms before averaging across epochs.

Between-state transitions. We examined between-state transitions (time periods when participants switch from one state to another): (1) initiation-to-maintenance transitions, where cooperators established a connection (≥2 s) from the initiation state and entered the maintenance state through connection points and (2) maintenance-to-initiation transitions, where cooperators failed to stay connected in the maintenance state and switched back to the initiation state through reset points. Our analysis focused on the time window before transition points (reset and connection points). Specifically, a 500-ms time window before each transition point was extracted as a transition epoch while data in the remaining periods were defined as nontransition periods. To reveal temporal profiles of cooperation behaviors during between-state transitions, we divided the data from nontransition periods into 500-ms time windows (nontransition epochs). As there were more nontransition epochs than transition ones, we randomly choose a number-matched subset of nontransition epochs for statistical analysis in Fig. 2g,i,k,m.

iEEG data analyses

Preprocessing of iEEG data. iEEG data were preprocessed using a pipeline similar to previous studies[60,61]. During offline preprocessing, the raw iEEG signals were first downsampled to 1,000 Hz and

bandpass-filtered between 1 and 150 Hz. To remove power-line noise, signals were bandstop-filtered at 50 ± 2 Hz and its harmonic frequencies using fourth-order Butterworth notch filters[60,61]. Channels underwent a quality check and were labeled as bad channels and discarded if they met any of the following criteria[60]: (1) located within the epileptic zone or severely contaminated by epileptic activity by visual inspection of the power spectrum and (2) variance greater than three times the mean variance across all channels during the entire task session. This step was repeated until no more bad channels were detected by the algorithm. All remaining channels were further visually inspected. The resulting signals of each channel were then rereferenced to the average activity across all clean channels[60,61,75].

To detect interictal epileptiform discharges (IEDs), we applied an automatic procedure using a double-thresholding algorithm[76]. iEEG signals were identified as IEDs if they met either of the following criteria and were subsequently excluded from further analyses: (1) the envelope of the unfiltered signal was four s.d. away from the baseline (that is, the average of the entire time series) and (2) the envelope of the filtered signal (bandpass-filtered at 25–80 Hz) was five s.d. away from the baseline. These steps were repeated until no more IEDs could be identified. Interictal spikes defined as 100-μV changes between successive samples[60] were also detected and labeled as IEDs. Additionally, we 'smoothed' detected IEDs by including an 800-ms time window around each IED (400 ms before and after), which was then discarded in all subsequent analyses. We omitted epochs containing IEDs when analyzing initiation and maintenance epochs. Finally, we visually inspected all channels for IEDs and removed those with excessive remaining artifacts.

We performed time–frequency analyses of iEEG signals for each channel using complex Morlet wavelets with adaptive cycles for individual frequency steps between 1 Hz and 150 Hz in 1-Hz steps[64] (linearly increasing from 3 (at 1 Hz) to 6 cycles (at 30 Hz) for the low-frequency range, from 6 (at 30 Hz) to 12 cycles (at 100 Hz) and holding at 12 cycles above frequencies exceeding 100 Hz). Subsequently, all power spectral data were downsampled to 100 Hz. Considering self-paced experimental design and varied trial lengths[50,63], we normalized the power separately for each frequency and channel using *z*-score transformation. Specifically, we subtracted the average power across the entire task session and divided it by the s.d. calculated across the same session's power.

Power during cooperation states. We investigated the spectrotemporal profiles of power for each cooperation state. First, we aggregated time–frequency data of power according to the cooperation state, separately for each recording channel. To reveal spectral properties, we averaged the power across all time points of each cooperation state for frequencies ranging from 4 to 150 Hz. For temporal properties, we used spectrotemporal maps of the 2-s initiation and maintenance epochs and averaged them across epochs for each cooperation state. For statistical inference, we compared power values against zero and between initiation and maintenance states across all recording channels for both spectral and temporal analyses. We determined the significance of power while correcting for multiple comparisons through nonparametric cluster-based permutation tests. To ensure an unbiased analysis with more stringent criteria, we further averaged power for each cooperation state across a broad gamma band (30–150 Hz), across all time points and recording channels per participant, resulting in a single broad gamma power value per participant. To visualize the time–frequency maps, we smoothed the power time series at each frequency by applying a one-dimensional Gaussian filter with a moving average window length of 250 ms before averaging it across epochs. Time–frequency maps were plotted at a temporal resolution of 10 ms. Power across the high-frequency band (30–150 Hz) significantly distinguished between the two cooperation states in both the amygdala and the TPJ (Fig. 3a,b), indicating its involvement in the cooperation dynamics. We then restricted our FOI to 30–150 Hz for subsequent intrabrain and interbrain analyses, aligning with previous hyperscanning studies where FOI was identified on the basis of functional relevance and interbrain correlations were calculated within the FOI[47–49].

Decoding of cooperation state transition. To test whether the high-frequency activity could forecast state transitions, we applied SVM to conduct the decoding analysis[77]. Specifically, binary SVM classifiers were trained to find the optimal hyperplane that distinguished patterns of high-frequency activity between two classes (between-state transition and nontransition). We trained separate classifiers for each cooperation state transition (initiation-to-maintenance and maintenance-to-initiation transitions) and for the amygdala and TPJ. Because of limited numbers of between-state transitions per participant, we applied the classifier using data across participants instead of building subject-wise decoding models. We used the MATLAB function 'fitcsvm' to train the classifier with a linear kernel and default hyperparameter settings. We applied tenfold cross-validation to minimize estimated errors and address the issue of overfitting.

As an illustration, we elaborate on the construction of the classifier for decoding initiation-to-maintenance transitions from nontransitions. We first computed the average power (30–150 Hz) across all recording channels within the same region for each participant, to account for varying channel numbers among participants. The resulting power was then aggregated across participants and organized into 200-ms time windows. We assigned class labels by designating each sample (the 200-ms window) as either a transition or nontransition. Time windows within the 2-s period around reset points were labeled as transition samples, while those outside this period in the initiation state were labeled as nontransition samples. Decoding models were built at intervals of every 40 ms starting 1 s before and ending 1 s after each state-transition point. We randomly selected a number-matched subset of nontransition samples to create a balanced training dataset.

For each model, high-frequency activity within the 200-ms time window was used as the feature, resulting in 20 features per model. Before pooling samples across participants, we normalized each feature across samples within each participant using *z*-score transformation to account for intersubject differences in neural activity levels. Using tenfold cross-validation, we randomly split the dataset into training and testing sets (9:1). The training and testing datasets were balanced for each class and the features of both datasets were separately normalized. Decoding accuracy was measured as the mean percentage of correctly labeled samples in the testing set across all folds. We repeated this procedure 500 times while considering randomization during dataset construction and cross-validation. A cluster-based permutation test was used to compare decoding accuracy to chance level across all repetitions. To better describe the decoding results, we reported the time points when significant decoding accuracy was observed, how long this significant decoding sustained and when optimal performance (peak accuracy) was achieved. The procedure for decoding maintenance-to-initiation transitions from nontransitions was identical except for data used in classifier training. In this analysis, time windows within the 2-s period around connection points were labeled as transition samples, while those outside this period in the maintenance state were labeled as nontransition samples. To gain the view of the features used in the decoding analysis, power time–frequency maps for each cooperation state-transition period are presented in Extended Data Fig. 4g–j.

Neural encoding of v_C and v_G. We performed neural–behavioral correlation analyses to examine how the cooperation elements (v_C and v_G) were encoded at the neuronal population level, covering the entire cooperation process. For each channel, we entered the time series of high-frequency power (30–150 Hz) into a multiple regression model that included v_C and v_G time series as two independent parametric

regressors. Partial correlation coefficients (β) were derived for v_C and v_G and then Fisher *z*-transformed. We assessed whether a given channel encoded either or both of these cooperation elements. Significance of encoding was determined using a permutation strategy[75,78]. Specifically, we shuffled the relationship between behavioral values and neural activity across time points for 5,000 independent times per regression model. We extracted the *F* statistics from the regression of each permutation to form a null distribution. The *P* value was obtained by calculating the proportion of surrogate *F* values equal to or greater than the observed *F* value. False discovery rate correction was applied to account for the number of channels for each brain region. This is a conservative approach. Channels were considered as v_C only if they significantly encoded v_C but not v_G and vice versa for v_G only channels. Some channels significantly encoded both v_C and v_G while nonencoding channels did not encode either v_C or v_G. For each brain region, encoding channels (v_C and/or v_G) were found in all session participants. To further explore state-specified encoding of cooperation elements, we repeated the above encoding analysis separately for each cooperation state but using power in the frequency bands from each cooperation state that significantly deviated from zero in a specific brain region (Fig. 3a,b).

Interbrain correlations

Calculation of interbrain correlation coefficient. To elucidate the interbrain relationship of iEEG signals between cooperating participants, we separately calculated correlation coefficients between activities of two interacting brains[50,51,79,80] at longer and shorter timescales. For long-range interbrain correlations, we aggregated power time–frequency data according to the cooperation state and averaged across the 30–150-Hz frequency band. For each region, we calculated Pearson correlation coefficients between time series of power across all channel pairs for each session dyad. The statistical significance was examined using one-sample *t*-tests above zero or paired *t*-tests between two states across all channel pairs after Fisher *z*-transformation of correlation coefficients and removal of outliers (±3 s.d.). To obtain spectral profiles of interbrain correlations in each state, we repeated the above procedure using power time series at individual frequencies from 30 to 150 Hz. Notably, we restricted our analysis only to positive interbrain correlations (indicating synchronized activity between two interacting brains) given that synchronized activity has been suggested to occur naturally and reflect social cognitive processes[81,82]. This also aligns with previous studies[44,51,80,83], which deemed only significantly increased (compared to baseline condition or zero) interbrain correlation as meaningful. Therefore, we only tested for significant positive correlations for all subsequent statistical analyses using one-sided statistical tests, including parametric (for example, *t*-tests in Fig. 5a,b) and nonparametric methods (for example, permutation test in Fig. 5c–f). To examine interbrain correlations at a finer temporal scale, we used a sliding window approach to calculate interbrain correlations within specific time windows (Supplementary Note 3 and Extended Data Fig. 6).

Relationship between interbrain correlations and cooperation behaviors. We investigated the potential associations between behavioral variables and interbrain correlations between cooperating teammates calculated using the sliding window method. For a specific region and cooperation state, we focused on frequency bands where interbrain correlation was significantly larger than zero (Fig. 5i–l). We first examined whether v_C and v_G were associated with interbrain correlations. We further examined behavioral synchrony represented as differences in v_C and v_G between teammates. Using the same method described above in the encoding analysis, we calculated partial correlation coefficients between interbrain correlations and v_C and v_G or their difference for each frequency band and channel pair individually. The statistical significance of resulting correlation coefficients was determined by conducting one-sample *t*-tests against zero across all channel pairs after removing outliers (±3 s.d.), FWE-corrected for the number of statistical tests (behavioral variables × number of frequency bands) within each cooperation state and brain region.

Statistical analysis

Statistical analyses of the preprocessed data were performed using MATLAB R2022a. All statistical tests were named and described with the corresponding results and sample sizes were clearly indicated. For parametric statistical tests (for example, *t*-tests and ANOVAs), data distribution was assumed to be normal but not formally tested. The *z*-score method was used to normalize the data to support the normality assumption. For analyses involving temporal or spectral clusters, significance was assessed using nonparametric cluster-based permutation tests (Supplementary Note 4). *P* values were adjusted for multiple comparisons using the FWE method where applicable. All statistical tests were two-sided tests unless otherwise specified. A significance level of 0.05 was used as the threshold for determining a statistically significant difference unless stated otherwise. Data are expressed as the mean ± 95% CI where relevant. No specific statistical methods were used to predetermine sample size.

Reporting summary

Further information on research design is available in the Nature Portfolio Reporting Summary linked to this article.

Data availability

The raw MRI and iEEG data containing personal information of the participants are protected and not available because of data privacy laws. Processed MRI and iEEG data are available with restricted access for ethical and privacy reasons. Access can be obtained from the corresponding author upon request. Supporting data are available online (https://osf.io/cjv9k/). The ICBM template brain (2009c) for channel visualization is publicly available online (https://nist.mni.mcgill.ca/icbm-152-nonlinear-atlases-2009/).

Code availability

The custom codes for the main analysis written in MATLAB are available online (https://osf.io/cjv9k/).

References

58. Zheng, J. et al. Multiplexing of theta and alpha rhythms in the amygdala–hippocampal circuit supports pattern separation of emotional information. *Neuron* **102**, 887–898 (2019).
59. Domenech, P., Rheims, S. & Koechlin, E. Neural mechanisms resolving exploitation–exploration dilemmas in the medial prefrontal cortex. *Science* **369**, eabb0184 (2020).
60. Kucyi, A. et al. Electrophysiological dynamics of antagonistic brain networks reflect attentional fluctuations. *Nat. Commun.* **11**, 325 (2020).
61. Liu, J. et al. Stable maintenance of multiple representational formats in human visual short-term memory. *Proc. Natl Acad. Sci. USA* **117**, 32329–32339 (2020).
62. Lopez-Persem, A. et al. Four core properties of the human brain valuation system demonstrated in intracranial signals. *Nat. Neurosci.* **23**, 664–675 (2020).
63. Stangl, M. et al. Boundary-anchored neural mechanisms of location-encoding for self and others. *Nature* **589**, 420–425 (2021).
64. Pacheco Estefan, D. et al. Coordinated representational reinstatement in the human hippocampus and lateral temporal cortex during episodic memory retrieval. *Nat. Commun.* **10**, 2255 (2019).
65. Gueguen, M. et al. Anatomical dissociation of intracerebral signals for reward and punishment prediction errors in humans. *Nat. Commun.* **12**, 3344 (2021).

66. Tan, H. et al. Intracranial EEG signals disentangle multi-areal neural dynamics of vicarious pain perception. *Nat. Commun.* **15**, 5203 (2024).
67. Brainard, D. H. The psychophysics toolbox. *Spat. Vis.* **10**, 433–436 (1997).
68. Stolk, A. et al. Integrated analysis of anatomical and electrophysiological human intracranial data. *Nat. Protoc.* **13**, 1699–1723 (2018).
69. Xia, M., Wang, J. & He, Y. BrainNet Viewer: a network visualization tool for human brain connectomics. *PLoS ONE* **8**, e68910 (2013).
70. Dale, A. M., Fischl, B. & Sereno, M. I. Cortical surface-based analysis: I. Segmentation and surface reconstruction. *Neuroimage* **9**, 179–194 (1999).
71. Friston, J. A. & Friston, K. Multimodal image coregistration and partitioning—a unified framework. *Neuroimage* **6**, 209–217 (1997).
72. Mobbs, D. et al. Promises and challenges of human computational ethology. *Neuron* **109**, 2224–2238 (2021).
73. Yoo, S. B. M., Tu, J. C., Piantadosi, S. T. & Hayden, B. Y. The neural basis of predictive pursuit. *Nat. Neurosci.* **23**, 252–259 (2020).
74. Treviño, M., Medina-Coss y León, R., Támez, S., Beltrán-Navarro, B. & Verdugo, J. Directional uncertainty in chase and escape dynamics. *J. Exp. Psychol. Gen.* **153**, 418–434 (2023).
75. Saez, I. et al. Encoding of multiple reward-related computations in transient and sustained high-frequency activity in human OFC. *Curr. Biol.* **28**, 2889–2899 (2018).
76. Gelinas, J. N., Khodagholy, D., Thesen, T., Devinsky, O. & Buzsáki, G. Interictal epileptiform discharges induce hippocampal–cortical coupling in temporal lobe epilepsy. *Nat. Med.* **22**, 641–648 (2016).
77. Pereira, F., Mitchell, T. & Botvinick, M. Machine learning classifiers and fMRI: a tutorial overview. *Neuroimage* **45**, S199–S209 (2009).
78. Marciano, D. et al. Electrophysiological signatures of inequity-dependent reward encoding in the human OFC. *Cell Rep.* **42**, 112865 (2023).
79. Kinreich, S., Djalovski, A., Kraus, L., Louzoun, Y. & Feldman, R. Brain-to-brain synchrony during naturalistic social interactions. *Sci. Rep.* **7**, 17060 (2017).
80. Abe, M. O. et al. Neural correlates of online cooperation during joint force production. *Neuroimage* **191**, 150–161 (2019).
81. Valencia, A. L. & Froese, T. What binds us? Inter-brain neural synchronization and its implications for theories of human consciousness. *Neurosci. Conscious.* **2020**, niaa010 (2020).
82. Schirmer, A., Fairhurst, M. & Hoehl, S. Being 'in sync'—is interactional synchrony the key to understanding the social brain? *Soc. Cogn. Affect. Neurosci.* **16**, 1–4 (2021).
83. Goldstein, P., Weissman-Fogel, I., Dumas, G. & Shamay-Tsoory, S. G. Brain-to-brain coupling during handholding is associated with pain reduction. *Proc. Natl Acad. Sci. USA* **115**, E2528–E2537 (2018).
84. Zhang, H., Fell, J. & Axmacher, N. Electrophysiological mechanisms of human memory consolidation. *Nat. Commun* . **9**, 4103 (2018).

Acknowledgements

This work was supported by the National Natural Science Foundation of China (projects 32125019 and 32430041 to Y.M.), STI-2030 Major Projects (2022ZD0211000 to Y.M.) and the Fundamental Research Funds for the Central Universities (2233300002 to Y.M.). We thank D. Wang and C. Hao for their assistance in data collection.

Author contributions

Y.M. conceptualized the project and designed the experiments. F.M., C.X., Y.Z., K.L., C.H., Y.G., X.Y., X.Z., J.N., H.T. and J.Y. performed the experiments and collected data. J.W. and Z.L. analyzed the data under the supervision of Y.M. J.W. and Y.M. wrote the original and final versions of the manuscript. All authors approved the final version of the manuscript for submission.

Competing interests

The authors declare no competing interests.

Additional information

Extended data is available for this paper at https://doi.org/10.1038/s41593-024-01824-y.

Supplementary information The online version contains supplementary material available at https://doi.org/10.1038/s41593-024-01824-y.

Correspondence and requests for materials should be addressed to Yina Ma.

Peer review information *Nature Neuroscience* thanks Kerstin Konrad, Josef Parvizi and the other, anonymous, reviewer(s) for their contribution to the peer review of this work.

https://doi.org/10.1038/s41593-024-01824-y

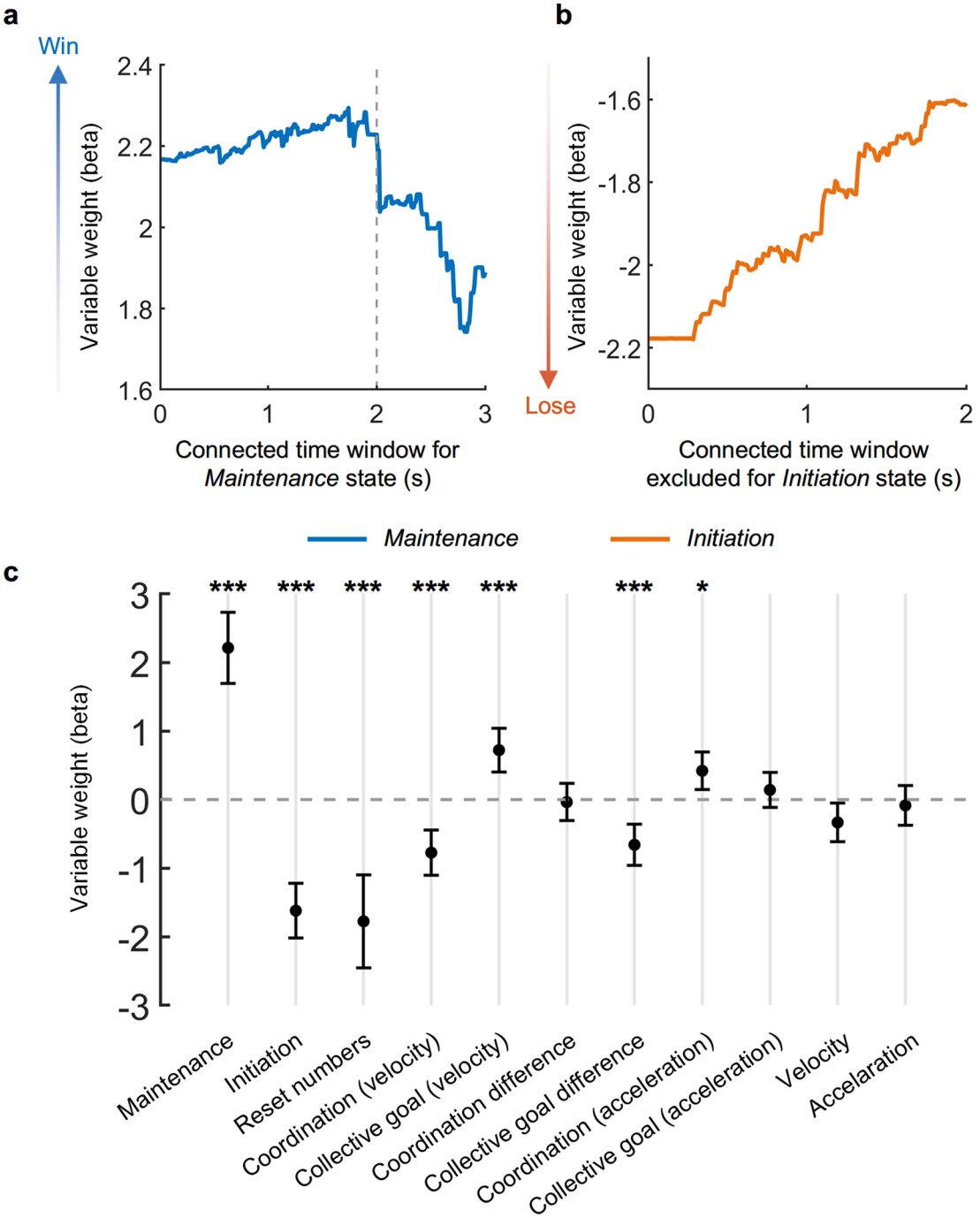

Extended Data Fig. 1 | See next page for caption.

https://doi.org/10.1038/s41593-024-01824-y

Extended Data Fig. 1 | The impact of behavioral variables on trial outcome. Linear mixed effect models are used for analysis. The response variable (trial outcome) was code as a categorical variable (1 for win and 0 for loss). Each behavioral variable (as a predictor) was z-scored across trials before model fitting. **a**, Impact of *maintenance* state (indicated by the percentage of time in the *maintenance* state in a trial) on trial outcome against different duration criteria for defining *maintenance* state. For example, under a 1-s criterion, *maintenance* state referred to time windows when teammate avatars maintained *connected* for at least 1 s. Larger beta weights indicate a stronger predictive effect on trial success. *Maintenance* state is defined as teammate avatars maintaining connected for at least 2 s due to the observed dramatic decrease in beta values after this 2-s criterion (dashed line), and sufficient duration to investigate behavioral dynamics. **b**, Impact of *initiation* state (indicated by the percentage of time in the *initiation* state in a trial) on trial outcome against different duration criteria used to exclude connected time-points within the remaining trial time after defining *maintenance* state based on the 2-s criterion. For example, under a 1-s criterion, we removed all time-points in which avatars are connected equal or less than 1 s within the remaining trial time to define *initiation* state. Smaller beta weights indicate stronger predictive effect on trial failure. Therefore, *initiation* state is defined as the time periods apart from the *maintenance* state in a trial (no further removal of connected time points). The *p* values associated with each beta value are FWE-corrected for multiple time criteria and show significance across all criteria (**a**, **b**, $p_{FWE} < 0.001$). **c**, Impact of behavioral variables of interest on trial win/lose. Logistic mixed-effect models were constructed to quantify the impact of each behavioral variable on cooperation by using trial outcome as the binary response variable and each behavioral index as an independent predictor. Behavioral predictors include: i) percentage of time spent in *maintenance* state, ii) percentage of time spent in *initiation* state, iii) the number of *resets*, iv) velocity-based coordination v_C, v) velocity-based collective goal pursuit v_G, vi) differences in v_C between teammate avatars, and vii) differences in v_G between teammate avatars. Additionally, we explored other variables that may contribute to cooperation by calculating avatar acceleration using second-order derivation of the position vector with respect to time, xiii) acceleration-based coordination, and ix) acceleration-based collective goal pursuit. We also calculated x) magnitudes of velocity at team center and xi) magnitudes of acceleration at team center. We aggregated trials from all patient dyads and calculated the above behavioral indices for each trial ($n = 270$). For time series variables such as velocity and acceleration, we averaged the value across all time points in each trial. We then normalized for each behavioral variable across trials as a fixed-effect variable and treated dyad and its interaction with trial number as two random-effect variables. We built individual models for each behavioral variable to estimate their independent impact on cooperation outcome while correcting for multiple comparisons using FWE to adjust *p* values. We showed that longer time spent in *maintenance* state increased the likelihood of winning the trial ($t_{268} = 8.359$, $p_{FWE} = 3.831 \times 10^{-14}$, $R_{adj}^2 = 0.728$, 95% CI: 1.692, 2.734), while longer time spent in *initiation* state decreased it ($t_{268} = -8.027$, $p_{FWE} = 3.478 \times 10^{-13}$, $R_{adj}^2 = 0.533$, 95% CI: -2.018, -1.223). A higher number of *reset* events in a trial may lead to losing it ($t_{268} = -5.159$, $p_{FWE} = 5.330 \times 10^{-6}$, $R_{adj}^2 = 0.222$, 95% CI: -2.453, -1.098). Larger velocity toward the team center (v_C) negatively predicted trial outcome ($t_{268} = -4.656$, $p_{FWE} = 5.595 \times 10^{-5}$, $R_{adj}^2 = 0.215$, 95% CI: -1.101, -0.447), whereas larger velocity toward the finish line (v_G) positively predicted trial outcome ($t_{268} = 4.476$, $p_{FWE} = 1.240 \times 10^{-4}$, $R_{adj}^2 = 0.196$, 95% CI: 0.404, 1.039), indicating that excessive focus on coordination could hinder reaching the finish line. Higher between-teammate movement synchrony toward the finish line predicted trial outcome (collective goal difference: $t_{168} = -4.327$, $p_{FWE} = 2.353 \times 10^{-4}$, $R_{adj}^2 = 0.138$, 95% CI: -0.960, -0.359). Additionally, we found a relatively weak positive impact of acceleration toward the team on trial outcome ($t_{268} = 3.005$, $p_{FWE} = 0.032$, $R_{adj}^2 = 0.086$, 95% CI: 0.145, 0.695). Data are mean ± 95% *CI*. Statistical tests are two-sided. Asterisks denote a significant difference ($^{*}p < 0.05$, $^{***}p < 0.001$, FWE-corrected for multiple comparisons).

https://doi.org/10.1038/s41593-024-01824-y

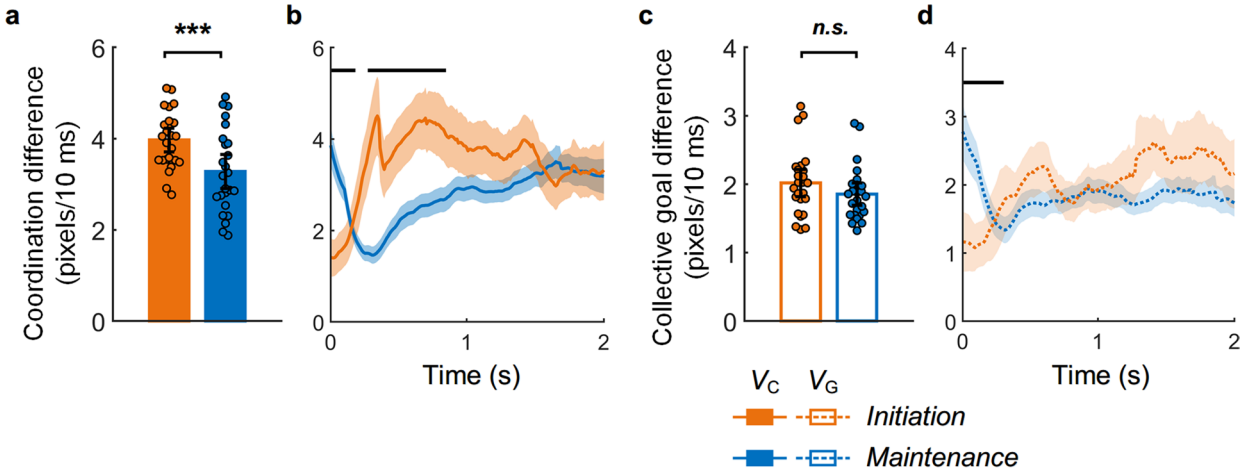

Extended Data Fig. 2 | Higher behavioral synchrony during cooperation maintenance. a, **b**, Comparisons of teammate coordination between *initiation* and *maintenance* states, averaged across the entire task session (**a**) and for each time-point of 2-s epochs (**b**). v_C differences were smaller in *maintenance* than *initiation* states (**a**, t_{14} = -3.968, $p = 5.715 \times 10^{-4}$, Cohen's d = 0.862, 95% CI: -1.052, -0.332, paired t-test), particularly during 280-850 ms time-window (**b**, $p_{corr} < 0.05$), suggesting that teammates exhibited better synchrony in moving towards teammate during cooperation maintenance. **c**,**d**, Same as (**a**) and (**b**), for collective goal pursuit. v_G differences were comparable in *initiation* and *maintenance* states (**c**, t_{24} = -1.362, p = 0.186, Cohen's d = 0.356, 95% CI: -0.408, 0.084, paired t-test; **d**, $p_{corr} < 0.05$), indicating a state-independent synchrony in pursuit of collective goals. Additionally, we observed poor synchrony in both movement towards teammate (**b**, v_C differences from onset to 190 ms) and the finish line (**d**, v_G differences from onset to 310 ms) at an early time-window of the *maintenance* state, possibly due to an *initiation*-to-*maintenance* transition effect. Given that there were more *maintenance* epochs than *initiation* ones, we randomly choose a number-matched subset of *initiation* epochs for statistical analysis in **b** and **d**. For visualization (**b**) and (**d**), behavioral time series were smoothed using a moving average window of 200 ms and averaged across epochs, with black horizontal lines indicating significant temporal clusters in two-sided permutation tests, corrected for multiple comparisons at the cluster level ($p_{corr} < 0.05$, n = 10000). Data are mean ± 95% *CI*. Overlaid dots represent session dyads (n = 25). Statistical tests are two-sided. $^{***}p < 0.001$.

https://doi.org/10.1038/s41593-024-01824-y

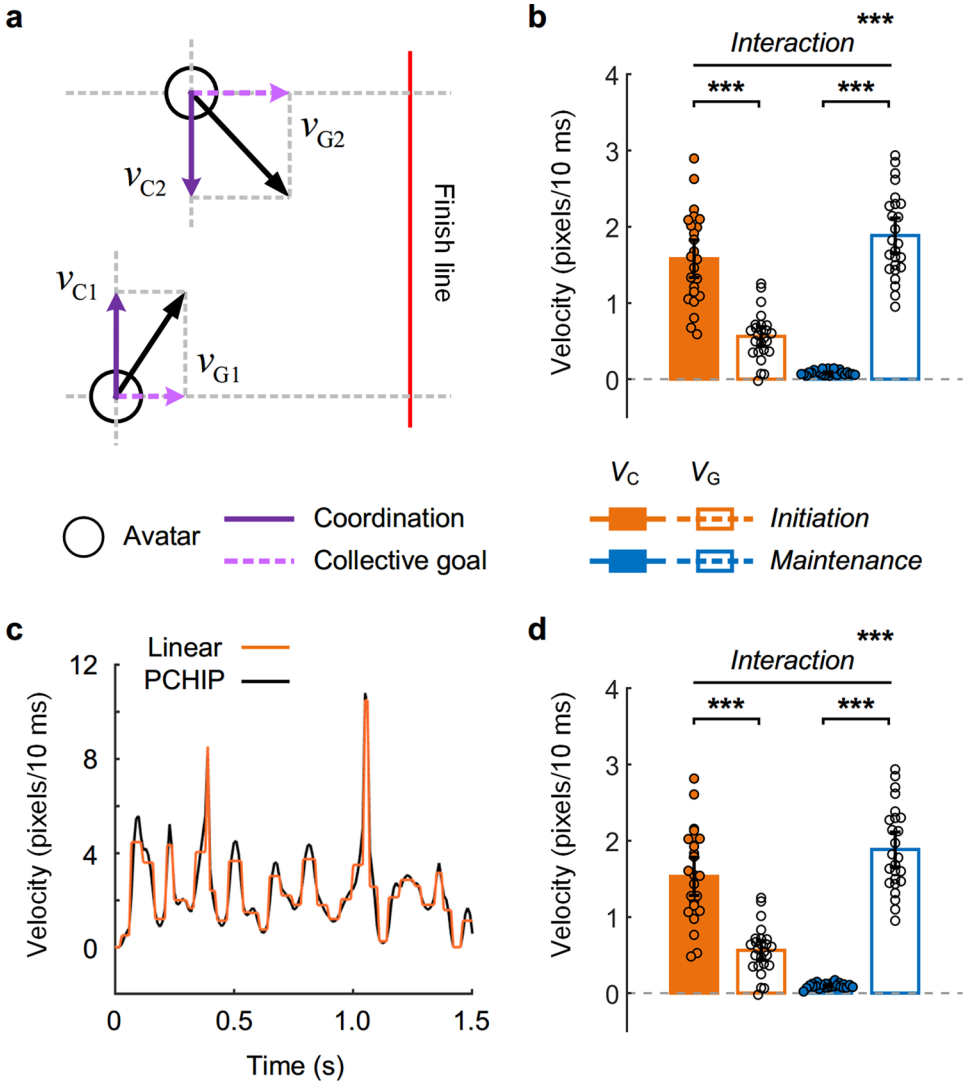

Extended Data Fig. 3 | Behavioral control analysis. a, Orthogonal decomposition of v_C and v_G. To quantify team coordination and collective goal pursuit, we employed an alternative approach of decomposing velocity onto the *x* axis and *y* axis to define v_C and v_G. We define the positive direction of *x* as pointing towards the finish line, and the positive direction of *y* as pointing towards the teammate's side. This decomposition method enables orthogonalization of v_C and v_G. **b**, By applying the decomposition method as described in (**a**), we have identified a significant interaction between *Velocity* and *State* ($F_{1,24} = 316.448$, $p = 2.511 \times 10^{-15}$, $\eta_p^2 = 0.930$, 90% CI: 0.870, 0.950, ANOVA of repeated-measurement), with v_C dominating the *initiation* state ($v_C > v_G$: $t_{24} = 8.266$, $p = 1.760 \times 10^{-8}$, Cohen's $d = 2.068$, 95% CI: 0.764, 1.273, paired *t*-test) and v_G dominating the *maintenance* state ($v_C < v_G$: $t_{24} = -16.893$, $p = 7.947 \times 10^{-15}$, Cohen's $d = 4.445$, 95% CI: -2.022, -1.582). **c**, We used linear interpolation and shape-preserving Piecewise Cubic Hermite Interpolating Polynomial (PCHIP) to interpolate the original trajectories (time series of *x* and *y* positions). The PCHIP method ensures continuity of velocity data while also preventing overshoots of data at flat regions. Shown here are examples of velocity temporal traces using both linear and PCHIP methods. **d**, Similarly, using the PCHIP method, we again observed the significant *Velocity* × *State* interaction ($F_{1,24} = 283.466$, $p = 8.561 \times 10^{-15}$, $\eta_p^2 = 0.922$, 90% CI: 0.856, 0.945, ANOVA of repeated-measurement). During the *initiation* state, v_C dominated ($v_C > v_G$: $t_{24} = 7.696$, $p = 6.221 \times 10^{-8}$, Cohen's $d = 1.957$, 95% CI: 0.710, 1.231, paired *t*-test), while during the *maintenance* state, v_G was dominant ($v_C < v_G$: $t_{24} = -16.757$, $p = 9.514 \times 10^{-15}$, Cohen's $d = 4.412$, 95% CI: -2.009, -1.568). Data are mean ± 95% *CI*. Overlaid dots represent session dyads ($n = 25$). Statistical tests are two-sided. $^{***}p < 0.001$.

https://doi.org/10.1038/s41593-024-01824-y

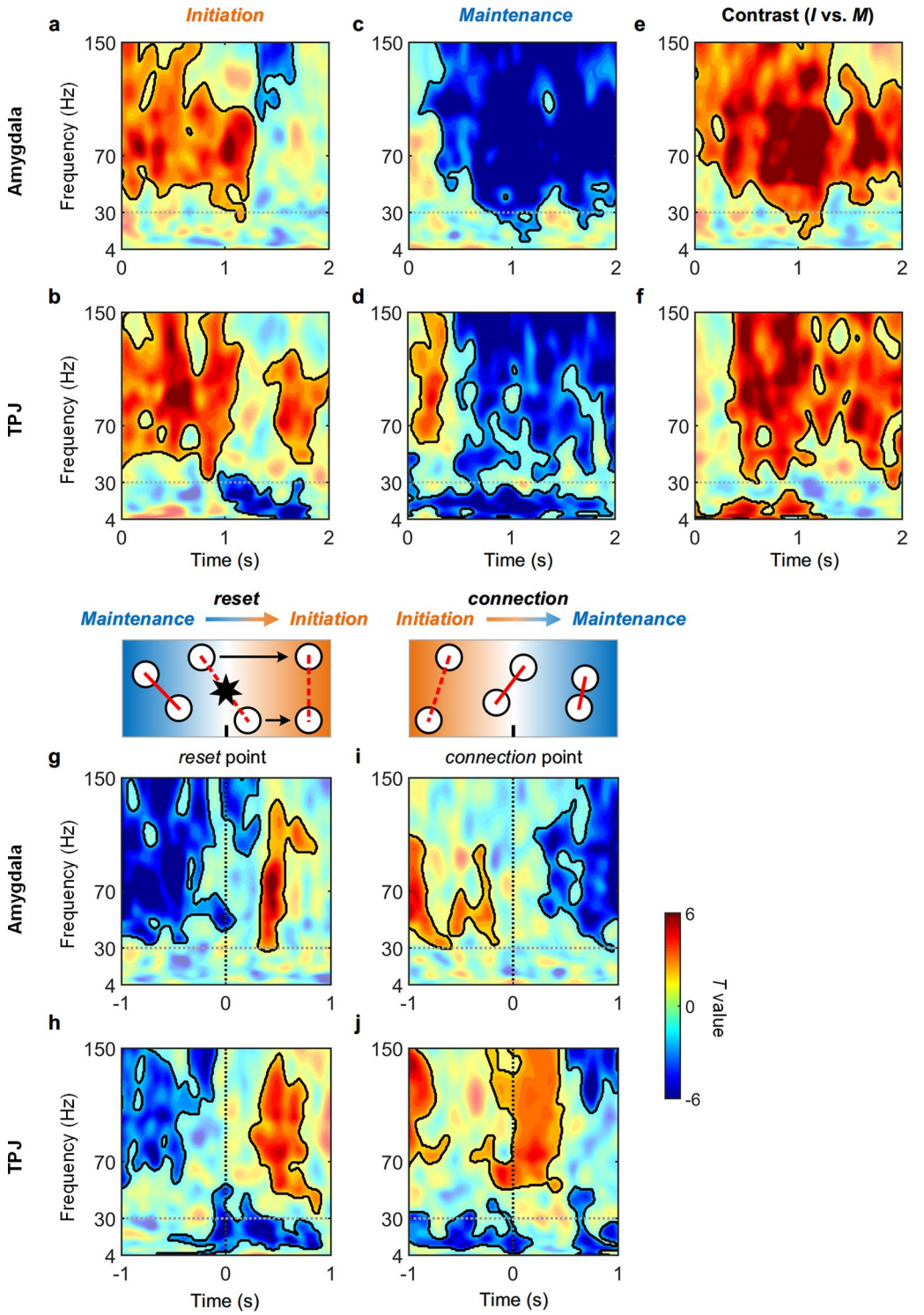

Extended Data Fig. 4 | See next page for caption.

https://doi.org/10.1038/s41593-024-01824-y

Extended Data Fig. 4 | The time-frequency spectrograms of oscillatory power. a-f, Time-frequency spectrograms (*t*-value maps) across 4-150 Hz for *initiation* state (**a**, **b**), *maintenance* state (**c**, **d**), between-state contrast (**e**, **f**) in the amygdala/TPJ. *Initiation* state exhibited increased power, covering broad gamma and high-gamma bands, in both the amygdala (**a**, from *initiation* onset and lasted up to 1290 ms, between 24-150 Hz) and TPJ (**b**, one significant cluster between onset and 1170 ms, 30-150 Hz; another 1380-2000 ms and 41-120 Hz). In addition, we found decreased power in the low frequency band (4-30 Hz) between 940 ms to 1820 ms in the TPJ. M*aintenance* state was featured with significant power decreases across a broad frequency range (**c**, amygdala: beginning 110 ms after the *maintenance* onset, between 10-150 Hz; **d**, TPJ: from 450 ms after the *maintenance* onset above 30 Hz and extending the whole *maintenance* epoch below 30 Hz). A positive cluster was also found in TPJ from 40 ms to 390 ms and between 58-150 Hz, possibly due to the transition effect. Direct comparisons of high-frequency power between *initiation* and *maintenance* states revealed significant clusters covering a broad frequency band in the amygdala (**e**, a cluster extending the whole epoch between 12-150 Hz) and in the TPJ (**f**, a cluster from epoch onset to 1270 ms at a lower frequency band of 4-24 Hz, another cluster from 310 ms to 2000 ms at the high frequency band of 26-150 Hz). **g-j**, Time-frequency spectrograms across 4-150 Hz of 2 s around state transition points of *reset* (**g**, **h**) and *connection* (**i**, **j**) for the amygdala/TPJ. During *maintenance*-to-*initiation* transition, we observed activity changes from decreased to increased power within gamma and high-gamma bands in the amygdala (**g**, negative power clusters lasted up to 320 ms before *reset* points, between 33-150 Hz; a positive power cluster occurring 310 ms after *reset* points, between 28-134 Hz) and TPJ (**h**, a negative cluster lasted up to 90 ms before *reset* points, between 52-150 Hz; a positive power cluster occurring 230 ms after *reset* points, between 34-146 Hz). In addition, a negative cluster was observed from 650 ms prior to *reset* points to 910 ms after *reset* points in across a lower frequency band of 4-54 Hz. During *initiation*-to-*maintenance* transition, we observed an opposite pattern of activity, which changed from increased to decreased power within gamma and high-gamma bands in the amygdala (**i**, positive clusters from 1000 to 140 ms prior to *connection* points, between 30-100 Hz; a negative cluster from 200 ms to 1000 ms after *connection* points, between 28-150 Hz) and the TPJ (**j**, positive clusters from 1000 prior to *connection* points to 480 ms after *connection* points, between 49-150 Hz; a negative cluster from 510 ms to 1000 ms after *connection* points, at high-gamma band of 105-150 Hz). We also found decreased power at the lower frequency band before and after transition in TPJ (a cluster from 1000 prior to *connection* points to 180 ms after *connection* points, between 6-46 Hz; another from 530 ms to 2000 ms after *connection* points, between 4-52 Hz). For display purposes, heat maps were smoothed by convolving power time series with a moving Gaussian window of 250 ms for each frequency bin. Black contours delimit significant clusters after two-sided cluster-based permutation tests ($p_{corr} < 0.05$, $n = 10000$).

https://doi.org/10.1038/s41593-024-01824-y

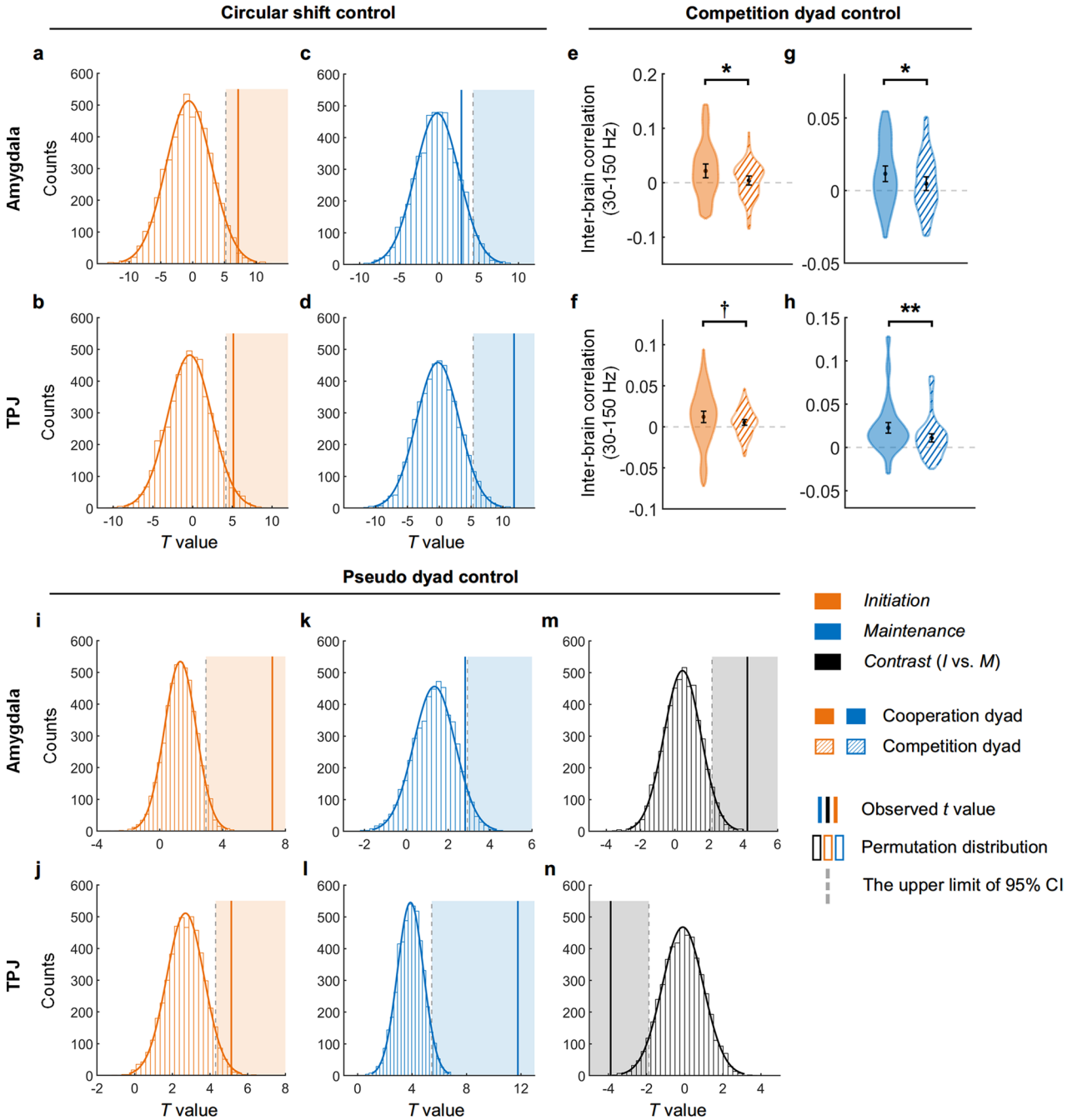

Extended Data Fig. 5 | Control analyses confirmed inter-brain neural correlations. We conducted a series of control analyses to validate the findings of inter-brain neural correlations (Supplementary Note 3). **a-d**, Circular shifted control. The *t* value of actual inter-brain correlations (in 30-150 Hz) for each state were compared against null distributions of *t* statistics created from the correlations of circularly shifted data between cooperators. We found increased inter-brain neural correlation of the actual data compared to that of circularly shifted data for both the amygdala (especially in the *initiation* state: $p = 0.012$, **a**; similar increasing trend in the *maintenance* state, $p = 0.149$, **c**) and TPJ (*initiation*: $p = 0.027$, **b**; *maintenance*: $p < 2 \times 10^{-4}$, **d**). **e-h**, Competition dyad as a control condition. We calculated the inter-brain correlation between competitors and compared it with that of cooperators. We found higher inter-brain correlations between cooperators than competition dyads during both the *initiation* (**e**, amygdala: $t_{64} = 2.477$, $p = 0.016$, Cohen's $d = 0.403$, 95% CI: 0.003, 0.032; **f**, TPJ: $t_{95} = 1.910$, $p = 0.059$, Cohen's $d = 0.258$, 95% CI: -2.803×10^{-4}, 0.015) and *maintenance* states (**g**, amygdala: $t_{65} = 2.040$, $p = 0.045$, Cohen's $d = 0.347$, 95% CI: 1.529×10^{-4}, 0.014; **h**, TPJ: $t_{92} = 3.322$, $p = 0.001$, Cohen's $d = 0.435$, 95% CI: 0.005, 0.190). Probability distributions of correlation coefficients for each channel (amygdala: $n = 67$, TPJ: $n = 97$) are shown as violin plots with black dots representing the mean and error bars representing 95% *CI*. Correlation coefficients were Fisher-transformed, and coefficient outliers (mean ± 3 s.d.) were excluded prior to statistical tests. Two-sided paired *t*-tests were used. **i-n**, Pseudo dyad control. The *t* value of real-interacting cooperators' inter-brain correlations (in 30-150 Hz) for each state and state difference were compared against null distributions of *t* statistics calculated from neural correlations between pseudo dyads. The significant inter-brain neural correlations in the amygdala and TPJ were replicated during both *initiation* (**i**, amygdala: $p < 2 \times 10^{-4}$; **j**, TPJ: $p = 0.005$) and *maintenance* states (**k**, amygdala: $p = 0.063$; **l**, TPJ: $p < 2 \times 10^{-4}$). Moreover, the inter-brain neural correlations in the amygdala showed a significant increase during *initiation* than *maintenance* states (**m**, amygdala: $p < 2 \times 10^{-4}$), while TPJ showed an opposite pattern with larger correlation in the *maintenance* state than *initiation* state (**n**, TPJ: $p < 2 \times 10^{-4}$). In **a-d** and **i-n**, vertical solid lines and dashed lines indicate observed inter-brain correlations and the upper/lower 95% CI of the null distributions (one-sided non-parametric permutation tests). Asterisks denote a significant difference ($^{\dagger}p < 0.10$, $^{*}p < 0.05$, $^{**}p < 0.01$, uncorrected).

https://doi.org/10.1038/s41593-024-01824-y

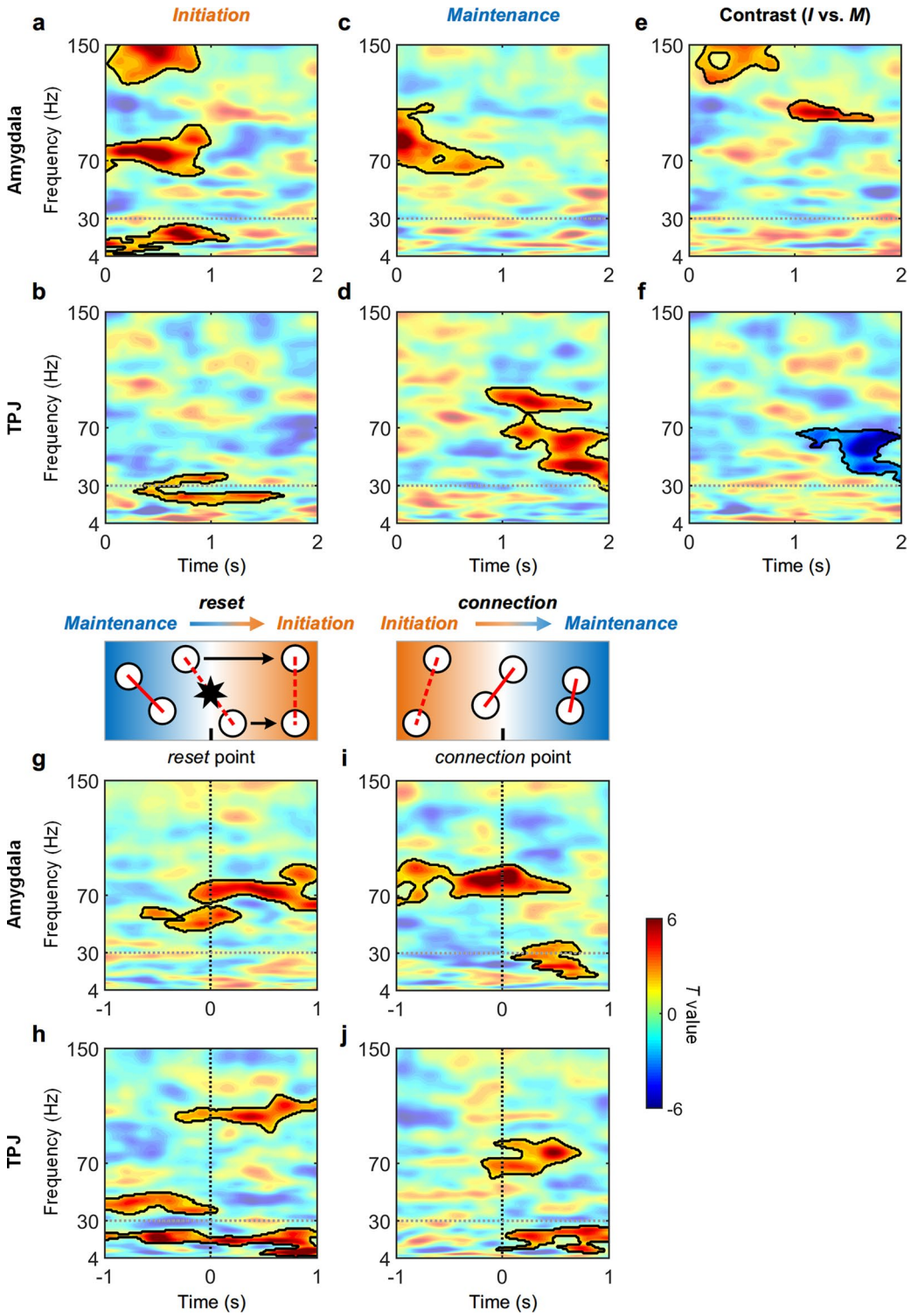

Extended Data Fig. 6 | See next page for caption.

https://doi.org/10.1038/s41593-024-01824-y

Extended Data Fig. 6 | The time-frequency spectrograms (*t*-value maps) of inter-brain neural correlations. a-f, Inter-brain neural correlation spectrograms are calculated across 4-150 Hz using sliding window method with a 500 ms sliding window and incremental steps of 10 ms (Supplementary Note 3) for the *initiation* state (**a**, **b**), *maintenance* state (**c**, **d**), and state contrast (**e**, **f**) for the amygdala/TPJ. During the *initiation* state, we observed clusters exhibiting a significant increase in inter-brain neural correlation within high-gamma bands (**a**, a cluster from epoch onset to 990 ms, ranging between 60 Hz to 94 Hz; another cluster from 30 ms to 890 ms, ranging between 123 Hz to 150 Hz) and within alpha and beta frequencies (from onset to 1160 ms, ranging between 4 Hz to 26 Hz) in the amygdala. A significant cluster at beta and lower gamma band were found in TPJ (**b**, from 280 ms to 1680 ms, ranging between 17 Hz to 38 Hz). During the cooperation *maintenance* state, we observed clusters with significantly increased inter-brain neural correlation in the gamma band in the amygdala (**c**, an early cluster from epoch onset to 1000 ms, ranging between 61 Hz to 109 Hz) and in TPJ (**d**, a cluster from 850 ms to 1830 ms, between 81 Hz to 97 Hz, another cluster from 990 ms to 2000 ms, between 27 Hz to 79 Hz). The comparison of spectro-temporal maps between the *initiation* and *maintenance* states revealed positive clusters in the high-gamma band in the amygdala (**e**, stronger inter-brain correlation during *initiation*, occurring between 80 ms to 840 ms at a frequency range of 124 Hz to 150 Hz, and between 940 ms to 1730 ms at a frequency range of between 98 Hz to 111 Hz) but negative clusters at the lower high-gamma band in TPJ (**f**, higher inter-brain neural correlation during *maintenance* state occurring between 1020 ms and 2000 ms at a frequency range of between 33 Hz to 69 Hz). Our results showed that the state-dependent inter-brain correlations were reliably observed at millisecond timescales, but exhibited region-specific patterns with opposite trends in the amygdala and TPJ. **g-j**, Inter-brain neural correlation spectrograms across 4-150 Hz of 2 s around state transition points of *reset* (**g**, **h**) and *connection* (**i**, **j**) for the amygdala/TPJ. During transition from *maintenance* state to *initiation* state, we observed clusters exhibiting significant inter-brain neural correlation within gamma and high-gamma bands in the amygdala (**g**, from 650 ms prior to *reset* points to 1000 ms after *reset* points, between 45 Hz and 91 Hz) and TPJ (**h**, a cluster from 1000 ms before *reset* points to 60 ms after *reset* points, between 35 Hz to 49 Hz; another cluster from 320 ms before *reset* points to 1000 ms after *reset* points, between 92 Hz to 117 Hz). A cluster extending the whole transition period was also found within alpha and beta bands in TPJ (from 6 Hz to 25 Hz). During transition from *initiation* state to *maintenance* state, we observed positive clusters of inter-brain neural correlation within the high-gamma band (**i**, from 1000 ms prior to *connection* points to 630 ms after *connection* points, between 64 Hz and 95 Hz) and the lower frequency band (90 ms to 890 ms after *connection* points, between 13 Hz and 38 Hz) in the amygdala. Results also revealed positive clusters of inter-brain neural correlation in the gamma band (**j**, from 190 ms prior to *connection* points to 730 ms after *connection* points, between 60 Hz and 87 Hz) and across alpha and beta bands (from 50 ms prior to *connection* points to 1000 ms after *connection* points, between 8 Hz and 26 Hz) in the TPJ. Our results suggested co-fluctuation of increased or decreased neural activity between cooperators during state transitions, prominently at the high-frequency band. The significant inter-brain correlation occurred temporally early than the transition points, suggesting that activities were also synchronized in predicting the upcoming transition events. During state transitions, inter-brain correlation might play an important role in updating and exchanging social information about the upcoming transition between cooperators. In **e** and **f**, significant clusters were identified from the observed data through two statistical comparisons[84]. First, we compared time-frequency maps of inter-brain correlation against zero for *initiation* and *maintenance* states separately, and extracted significant clusters with positive *t*-values under a single condition. Then, we compared time-frequency maps of inter-brain correlation between *initiation* and *maintenance* states and extracted significant clusters under condition contrast. New clusters were obtained by calculating the intersection of significant clusters from both comparisons, which were further statistically compared with the null distribution from the second comparison to obtain corrected *p*-values for each cluster. These procedures ensured that significant between-state differences in inter-brain correlations were also reliably larger than zero in each state. For display purposes, heat maps were smoothed by convolving inter-brain correlation time series with a moving Gaussian window of 250 ms for each frequency bin. Black contours delimit significant clusters after cluster-based permutation tests ($n = 10000$). In **a**-**d** and **g**-**j**, we used one-sided test with a threshold of $p_{corr} < 0.05$. In **e** and **f**, we used two-sided test with a threshold $p_{corr} < 0.05$.

https://doi.org/10.1038/s41593-024-01824-y

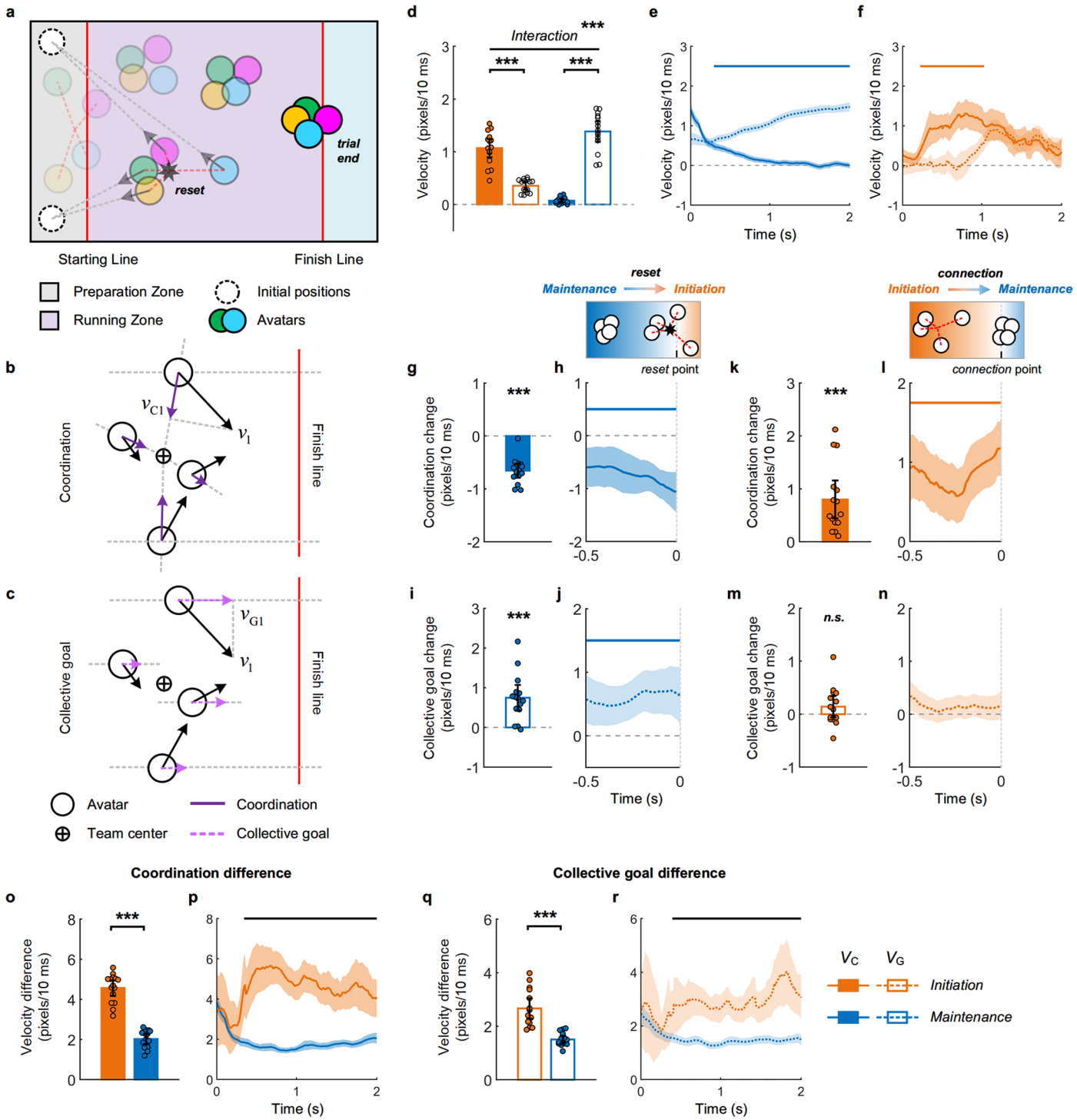

Extended Data Fig. 7 | See next page for caption.

https://doi.org/10.1038/s41593-024-01824-y

Extended Data Fig. 7 | The behavioral results of the 4-person team, non-competitive *cooperative running game*. **a**, A schematic representation of the virtual *cooperative running game*. In this task, there is only one 4-person team, aiming to cross the finish line together but without any competitive pressure. The four avatars in this game are of different shapes and colors (blue triangle, orange rectangle, purple diamond, and green pentagon), allowing participants to easily identify themselves. The initial positions of these avatars are predetermined and remained unchanged throughout gameplay. For illustration purpose, the avatars are depicted as colored circles. Despite some modifications of game settings, this game inherited the fundamental principles of the 'three-legged' analogy. Prior to entering the *running* zone during each trial, avatars had to establish a connection with the other teammates when the distances between any two teammates are all below a preset safe distance (that is, $d_{ij} < 250$, where $d_{ij} \in \{d_{12}, d_{13}, d_{14}, d_{23}, d_{24}, d_{34}\}$). Note that we have slightly relaxed the safe distance threshold due to the increased challenge of maintaining connected among 4 participants. All other aspects of the game interface and procedures remain identical to those of the three-legged racing game. They proceed through the *running* zone towards the finish line while maintaining their connection, striving to move as fast as possible. However, if the connection is lost within the *running* zone, a *reset* event occurs and avatars must restart from the *preparation* zone. To illustrate this occurrence, we have used a dashed red line and an 'explosion' symbol to indicate where the connection is broken; these elements were not present in actual gameplay. **b**, **c**, We quantified team coordination (**b**, v_C averaged across four teammates) and collective goal pursuit (**c**, v_G averaged across four teammates) by decomposing avatars' velocity and projecting it onto the team center and the finish line, respectively. Specifically, velocities from all four teammate avatars were used to calculate v_C and v_G. Behavioral synchrony variables were calculated between each two teammates and averaged across pairs. Schematic illustration of v_{C1} and v_{G1} were shown in the panels as an example. **d**, *Initiation* and *maintenance* states were dominated by v_C and v_G, respectively. Teammate coordination dominated the *initiation* state ($v_C > v_G$: $t_{14} = 7.657$, $p = 2.273 \times 10^{-6}$, Cohen's $d = 2.808$, 95% CI: 0.514, 0.914, paired *t*-test). In contrast, moving toward the finish line dominated the *maintenance* state ($v_C < v_G$: $t_{14} = -15.681$, $p = 2.825 \times 10^{-10}$, Cohen's $d = 4.912$, 95% CI: -1.492, -1.133). A significant *Velocity* × *State* interaction ($F_{1,14} = 164.739$, $p = 3.926 \times 10^{-9}$, $\eta_p^2 = 0.922$, 90% CI: 0.817, 0.948, ANOVA of repeated-measurement) further confirmed this opposite pattern. **e**, **f**, Temporal profiles of v_C and v_G, as well as their contrast across the 2-s *maintenance* epochs (**e**) and *initiation* epochs (**f**), respectively. In the *maintenance* state, v_G was significantly larger than v_C for a long time period from 300 ms after onset ($p_{corr} < 0.05$). In the *initiation* state, v_G was lower than v_C especially in an early time window of 230-1030 ms (cluster-based permutation tests, $p_{corr} < 0.05$, $n = 10000$). **g**-**j**, Decreasing v_C (**g**, **h**) and increasing v_G (**i**, **j**) accounted for state transition from *maintenance* to *initiation*. We observed significant decreases in v_C (**g**, $t_{14} = -10.626$, $p = 4.379 \times 10^{-8}$, Cohen's $d = 2.594$, 95% CI: -0.789, -0.524, one-sample *t*-test) and significant increases in v_G (**i**, $t_{14} = 4.912$, $p = 2.290 \times 10^{-4}$, Cohen's $d = 1.120$, 95% CI: 0.420, 1.072, one-sample *t*-test) occurring 500 ms prior to the *reset* points, and covering the last 500-ms time window before transitions from *maintenance* to *initiation* states (relative to other stable *maintenance* periods, **h**, **j**, $p_{corr} < 0.05$). **k**-**n**, Increasing v_C (**k**, **l**) with unchanged v_G (**m**, **n**) contributed to state transition from *initiation* to *maintenance*. We found significant increases in v_C (**k**, $t_{14} = 4.780$, $p = 2.935 \times 10^{-4}$, Cohen's $d = 1.167$, 95% CI: 0.441, 1.158, one-sample *t*-test), covering the entire 500 ms before the *connection* point (**l**, $p_{corr} < 0.05$), without significant changes in v_G (**m**, $t_{14} = 1.496$, $p = 0.157$, Cohen's $d = 0.365$, 95% CI: -0.061, 0.341, one-sample *t*-test; **n**, $p_{corr} < 0.05$). **o**-**r**, Comparisons of teammate coordination (**o**, **p**) and collective goal pursuit (**q**, **r**) between *initiation* and *maintenance* states, averaged across the entire task session (**o**, **q**) and for each time point of 2-s epochs (**p**, **r**). Results showed smaller v_C differences (**o**, $t_{14} = -11.841$, $p = 1.110 \times 10^{-8}$, Cohen's $d = 4.111$, 95% CI: -2.992, -2.074, paired *t*-test) from 350 ms after epoch onset (**p**, $p_{corr} < 0.05$), and also smaller v_G differences (**q**, $t_{14} = -6.243$, $p = 2.151 \times 10^{-5}$, Cohen's $d = 2.120$, 95% CI: -1.555, -0.760, paired *t*-test) during the time window of 400 ms to 2000 ms (**r**, $p_{corr} < 0.05$) in the *maintenance* than the *initiation* states. We balanced the numbers of non-transition epochs and state-transition epochs in **h**, **j**, **l** and **n**, and also the numbers of *initiation* epochs and *maintenance* epochs in P and R for plotting and statistical testing (Methods). Data are mean ± 95% *CI*. Overlaid dots represent 4-person teams ($n = 15$). Statistical tests are two-sided. For visualization of behavioral temporal profiles, time series (**e**, **f**, **h**, **j**, **l**, **n**, **p** and **r**) were smoothed with a 200-ms moving average window, with horizontal colored bars indicating significant temporal clusters in permutation tests corrected for multiple comparisons at the cluster level ($p_{corr} < 0.05$, $n = 10000$). $^{***}p < 0.001$, *n.s.* not significant.

https://doi.org/10.1038/s41593-024-01824-y

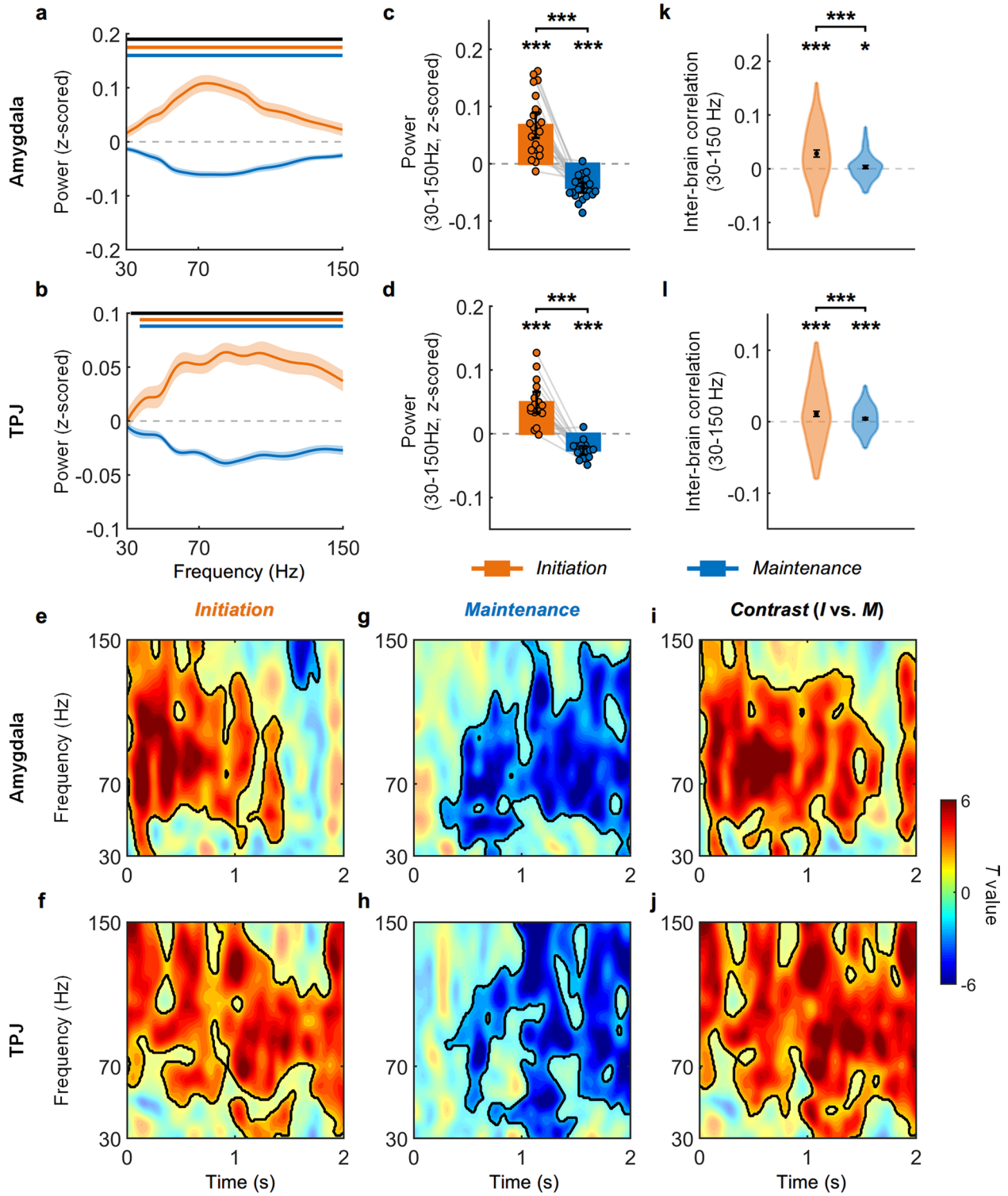

Extended Data Fig. 8 | See next page for caption.

https://doi.org/10.1038/s41593-024-01824-y

Extended Data Fig. 8 | The neural results of the 4-person team, non-competitive *cooperative running game*. **a**, **b**, Normalized power in the amygdala (**a**, $n = 103$ channels) and TPJ (**b**, $n = 162$ channels) during cooperation *initiation* and *maintenance* states plotted as a function of frequency. We replicated that *initiation* and *maintenance* states were differentiated by a significant difference in power in the 30 Hz to 150 Hz high-frequency band. This power difference was further confirmed by a significant power increase in the *initiation* state but a significant power decrease in the *maintenance* state within the 30-150 Hz frequency band. Horizontal orange, blue, and black bars indicate the significant frequency bands for the *initiation* state, *maintenance* state, and between-state contrast (cluster-based permutation tests, $p_{corr} < 0.05$, $n = 10000$). **c**, **d**, Normalized high-frequency power averaged between 30-150 Hz during *initiation* and *maintenance* states in the amygdala (**c**, $n = 23$ patients) and TPJ (**d**, $n = 18$ patients). The state-dependent high-frequency activity pattern was strikingly consistent across sessions in both amygdala (**c**, *initiation vs. maintenance*: $t_{22} = 8.160$, $p = 4.240 \times 10^{-8}$, Cohen's $d = 2.724$, 95% CI: 0.082, 0.137, paired *t*-test, consistent in 100% teams) and TPJ (**d**, *initiation vs. maintenance*: $t_{17} = 8.380$, $p = 1.929 \times 10^{-7}$, Cohen's $d = 2.858$, 95% CI: 0.056, 0.094, paired *t*-test, consistent in 94% teams). Specifically, we found significant power increases in the *initiation* state (amygdala: $t_{22} = 6.310$, $p = 2.380 \times 10^{-6}$, Cohen's $d = 1.270$, 95% CI: 0.045, 0.089; TPJ: $t_{17} = 6.337$, $p = 7.444 \times 10^{-6}$, Cohen's $d = 1.426$, 95% CI: 0.033, 0.066, one-sample *t*-tests) but power decreases in the *maintenance* state (amygdala: $t_{22} = -10.228$, $p = 7.995 \times 10^{-10}$, Cohen's $d = 2.059$, 95% CI: -0.051, -0.034; TPJ: $t_{17} = -8.210$, $p = 2.558 \times 10^{-7}$, Cohen's $d = 1.848$, 95% CI: -0.033, -0.019). Overlaid dots represent session participants. **e-j**, Time-frequency spectrograms (*t*-value maps) of epochs from *initiation* state (**e**, **f**), *maintenance* state (**g**, **h**), and between-state contrast (**i**,**j**) in the amygdala/TPJ. In the *initiation* state, we found clusters exhibiting power increases covering a broad frequency range of 30-150 Hz, in both the amygdala (**e**, significant clusters emerged at *initiation* onset and lasted up to 1440 ms) and TPJ (**f**, a significant cluster covering the entire 2000 ms epoch). In the cooperation *maintenance* state, there were significant power decreases across a broad frequency range of 30-150 Hz in both the amygdala (**g**, beginning 260 ms after the *maintenance* onset) and TPJ (**h**, from 300 ms after the *maintenance* onset). Direct comparisons of high-frequency power between *initiation* and *maintenance* states revealed significant clusters in amygdala (**i**, one cluster between onset and lasted up to 1690 ms, 30-150 Hz; another covering 1830-2000 ms and 39-142 Hz), and in TPJ (**j**, covering the entire 2000 ms epoch). For display purposes, power heat maps were smoothed by convolving power time series with a moving Gaussian window of 250 ms for each frequency bin. Black contours delimit significant clusters after two-sided cluster-based permutation tests ($p_{corr} < 0.05$, $n = 10000$). **k**,**l**, Inter-brain neural correlation (Pearson correlation coefficients) in 30-150 Hz between two interacting brains across all channel pairs in the amygdala (**k**, $n = 286$) and TPJ (**l**, $n = 555$), during *initiation* and *maintenance* states. The results replicated the findings in the *three-legged racing* game that the amygdala high-frequency power of the cooperating teammates was significantly correlated in the *initiation* state ($t_{282} = 8.656$, $p = 1.904 \times 10^{-16}$, Cohen's $d = 0.513$, lower 95% CI: 0.023, one-sided one-sample *t*-test) and the *maintenance* state ($t_{280} = 2.096$, $p = 0.018$, Cohen's $d = 0.125$, lower 95% CI: 0.001). The TPJ power in the 30-150 Hz band of two teammates was significantly correlated during both the *initiation* ($t_{553} = 5.858$, $p = 4.027 \times 10^{-9}$, Cohen's $d = 0.249$, lower 95% CI: 0.008) and *maintenance* states ($t_{550} = 5.017$, $p = 3.554 \times 10^{-7}$, Cohen's $d = 0.213$, lower 95% CI: 0.003). Inter-brain neural correlation also exhibited state-dependency, however, with stronger correlation during *initiation* than *maintenance* states in both amygdala ($t_{277} = -7.174$, $p = 6.655 \times 10^{-12}$, Cohen's $d = 0.591$, 95% CI: -0.032, -0.018, paired *t*-test) and TPJ ($t_{549} = -3.501$, $p = 5.005 \times 10^{-4}$, Cohen's $d = 0.201$, 95% CI: -0.011, -0.003). Correlation coefficients were Fisher-transformed. Data are mean ± 95% CI. In **k** and **l**, violin plots depict the probability distributions of inter-brain neural correlation across channel pairs, with black dots represent the mean. Prior to statistical tests, any correlation coefficient outliers (mean ± 3 s.d.) were excluded. Statistical tests are two-sided unless otherwise stated. $^{*}p < 0.05$, $^{***}p < 0.001$.

https://doi.org/10.1038/s41593-024-01824-y

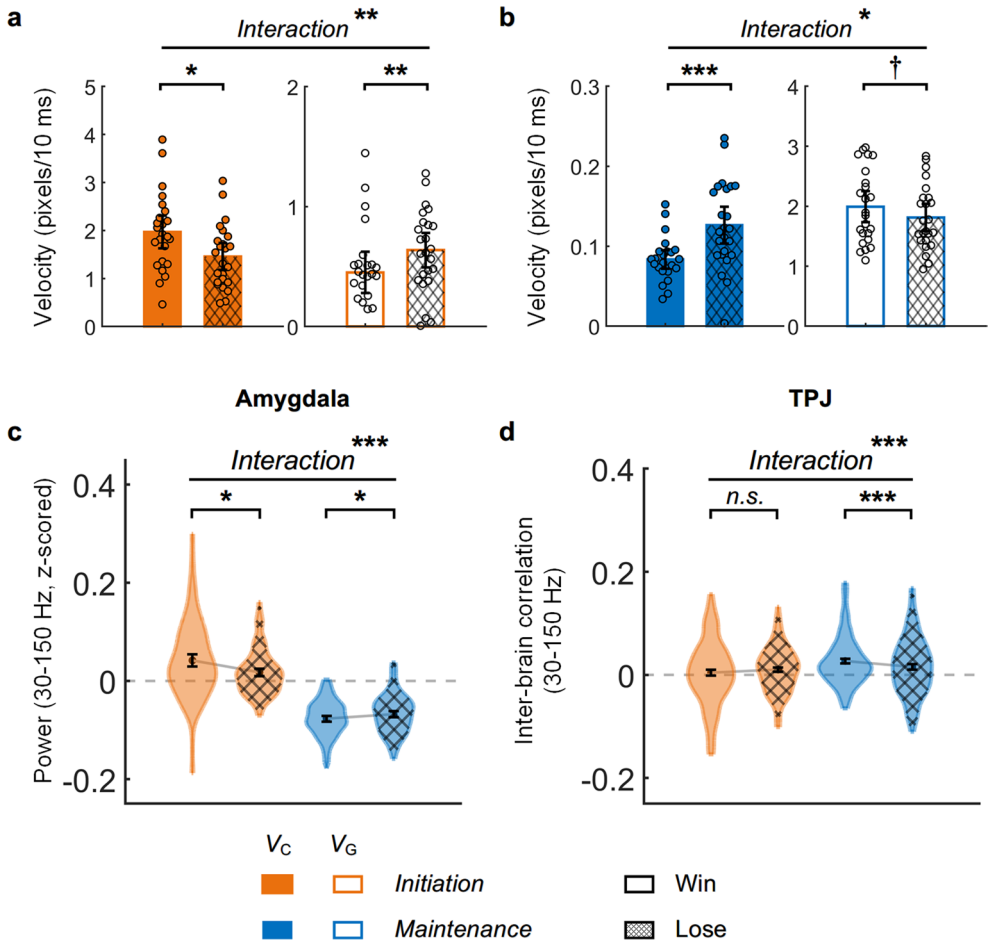

Extended Data Fig. 9 | Behavioral and neural profiles between win and loss trials. To examine whether the behavioral and neural profiles differed between win and loss trials, we performed ANOVAs on the behavioral and neural data, including the trial outcome as a within-subject independent variable. For the behavioral analysis, we conducted a three-way ANOVA of repeated measurement including *Velocity*, *State*, and *Outcome* as within-dyads variables. For the intra- and inter-brain analysis, we averaged high-frequency power (30-150 Hz), and calculated inter-brain correlation across win and loss trials respectively. We conducted two-way ANOVAs of repeated measurement for power and inter-brain correlation including *State* and *Outcome* as within-dyads variables. **a, b**, Behavioral results revealed a significant *Velocity* × *State* × *Outcome* three-way interaction, indicating stronger *Velocity* × *State* interaction for win trials than loss trials ($F_{1,22} = 13.897$, $p = 0.001$, $\eta_p^2 = 0.387$, 90% CI: 0.120, 0.564, ANOVA of repeated-measurement). Further decomposing the three-way interaction, we conducted ANOVA separately for each cooperation state and found significant *Velocity* × *Outcome* interaction in both *initiation* ($F_{1,22} = 10.526$, $p = 0.004$, $\eta_p^2 = 0.324$, 90% CI: 0.074, 0.514) and *maintenance* ($F_{1,22} = 5.117$, $p = 0.034$, $\eta_p^2 = 0.189$, 90% CI: 0.008, 0.397) states. Specifically, for *initiation* state (**a**), we found wining trials are featured by increased v_C ($t_{22} = 2.711$, $p = 0.013$, Cohen's $d = 0.657$, 95% CI: 0.117, 0.882) and decreased v_G ($t_{22} = -3.128$, $p = 0.005$, Cohen's $d = 0.536$, 95% CI: -0.345, -0.070), suggesting that during cooperation *initiation*, more focus on coordination and stronger suppression of collective goal pursuit contributed to wining the trial. For *maintenance* state (**b**), lower level of v_C ($t_{22} = -4.509$, $p = 1.738\times10^{-4}$, Cohen's $d = 0.536$, 95% CI: -0.345, -0.070) and a trend of higher v_G ($t_{22} = 1.848$, $p = 0.078$, Cohen's $d = 0.313$, 95% CI: -0.022, 0.383) were found in win trials compared to loss trials, indicating less concentration on teammate coordination and more effort exerted toward collective goal during cooperation *maintenance* facilitates winning the trial. These behavioral findings once again highlight the important role of teammate coordination in the success of cooperation. More engagement in interpersonal coordination during cooperation establishment, and less during cooperation maintenance enable cooperators to achieve cooperation more efficiently. **c**, Contrast of power between win and lose trials showed a significant *State* × *Outcome* interaction only in amygdala ($F_{1,156} = 15.069$, $p = 1.526\times10^{-4}$, $\eta_p^2 = 0.088$, 90% CI: 0.030, 0.164), but not in TPJ ($F_{1,229} = 0.348$, $p = 0.556$, $\eta_p^2 = 0.002$, 90% CI: 0.000, 0.021). We found that high-frequency band neural activity increased in *initiation* state ($t_{156} = 2.495$, $p = 0.014$, Cohen's $d = 0.296$, 95% CI: 0.004, 0.036) and decreased in *maintenance* state ($t_{156} = -2.470$, $p = 0.015$, Cohen's $d = 0.249$, 95% CI: -0.018, -0.002) for win trials compared with loss trials. **d**, For inter-brain correlation, we found a significant *State* × *Outcome* interaction only in TPJ ($F_{1,457} = 9.381$, $p = 0.002$, $\eta_p^2 = 0.020$, 90% CI: 0.004, 0.046), but not in amygdala ($F_{1,246} = 1.106$, $p = 0.294$, $\eta_p^2 = 0.004$, 90% CI: 0.000, 0.028). This interaction was mainly attributed to a significant larger inter-brain correlation at high-frequency band in *maintenance* state in win trials than loss trials ($t_{458} = 3.506$, $p = 5.002\times10^{-4}$, Cohen's $d = 0.228$, 95% CI: 0.005, 0.019). The result indicates that more synchronized TPJ activities between teammates during well-maintained cooperation contributed to higher efficiency and a satisfactory outcome. Together, these results suggested that the significant behavioral and neural patterns might facilitate efficient cooperation since these patterns were more prominent in winning trials than losing trials. In **a** and **b**, overlaid dots represent session dyads with both win and loss trials ($n = 23$). In **c** and **d**, violin plots depict the probability distributions of power or inter-brain neural correlation across channel (**c**, amygdala: $n = 157$) or channel pairs (**d**, TPJ, $n = 479$). Correlation coefficients were Fisher-transformed, and coefficient outliers (mean ± 3 s.d.) were excluded prior to statistical tests. ANOVA of repeated-measurement are used for multi-factor analyses. Paired *t*-tests are used for pair-wise comparisons. Data are mean ± 95% CI. Statistical tests are two-sided unless otherwise stated. $^{\dagger}p < 0.05$, $^{*}p < 0.05$, $^{**}p < 0.01$, $^{***}p < 0.001$, *n.s.* not significant.

nature portfolio

Corresponding author(s): Yina Ma

Last updated by author(s): Sep 6, 2024

Reporting Summary

Nature Portfolio wishes to improve the reproducibility of the work that we publish. This form provides structure for consistency and transparency in reporting. For further information on Nature Portfolio policies, see our Editorial Policies and the Editorial Policy Checklist.

Statistics

For all statistical analyses, confirm that the following items are present in the figure legend, table legend, main text, or Methods section.

n/a	Confirmed	
☐	☒	The exact sample size (*n*) for each experimental group/condition, given as a discrete number and unit of measurement
☐	☒	A statement on whether measurements were taken from distinct samples or whether the same sample was measured repeatedly
☐	☒	The statistical test(s) used AND whether they are one- or two-sided *Only common tests should be described solely by name; describe more complex techniques in the Methods section.*
☐	☒	A description of all covariates tested
☐	☒	A description of any assumptions or corrections, such as tests of normality and adjustment for multiple comparisons
☐	☒	A full description of the statistical parameters including central tendency (e.g. means) or other basic estimates (e.g. regression coefficient) AND variation (e.g. standard deviation) or associated estimates of uncertainty (e.g. confidence intervals)
☐	☒	For null hypothesis testing, the test statistic (e.g. *F*, *t*, *r*) with confidence intervals, effect sizes, degrees of freedom and *P* value noted *Give P values as exact values whenever suitable.*
☒	☐	For Bayesian analysis, information on the choice of priors and Markov chain Monte Carlo settings
☒	☐	For hierarchical and complex designs, identification of the appropriate level for tests and full reporting of outcomes
☐	☒	Estimates of effect sizes (e.g. Cohen's *d*, Pearson's *r*), indicating how they were calculated

Our web collection on statistics for biologists contains articles on many of the points above.

Software and code

Policy information about availability of computer code

Data collection	Behavioral data were collected using Psychophysics Toolbox Version 3 (PTB-3) extension in MATLAB R2016a (MathWorks). iEEG data were collected using Nicolet EEG system (Alliance Biomedica Pvt. Ltd., India), Nihon-Kohden system (Nihon Kohden Corporation Japan) and Micromed system (Micromed S.p.A., Italy).
Data analysis	Behavioral data were analyzed using custom codes in MATLAB R2022a. iEEG data were analyzed using FieldTrip (v20220310) implemented in MATLAB, and custom codes in MATLAB R2022a. Imaging data were processed using FieldTrip (v20220310), Freesurfer (v5.3.0), Statistical Parametric Mapping (SPM12) and visualized using BrainNet Viewer (v1.7). The custom codes for the main analysis written in MATLAB are available at https://osf.io/cjv9k/.

For manuscripts utilizing custom algorithms or software that are central to the research but not yet described in published literature, software must be made available to editors and reviewers. We strongly encourage code deposition in a community repository (e.g. GitHub). See the Nature Portfolio guidelines for submitting code & software for further information.

Data

Policy information about availability of data

All manuscripts must include a data availability statement. This statement should provide the following information, where applicable:

- Accession codes, unique identifiers, or web links for publicly available datasets
- A description of any restrictions on data availability
- For clinical datasets or third party data, please ensure that the statement adheres to our policy

The raw MRI and iEEG data that contain personal information of the patients are protected and not available due to data privacy laws. Processed MRI and iEEG data are available with restricted access for ethical and privacy reasons. Access can be obtained from the corresponding author upon request. Source data are available at https://osf.io/cjv9k/. The ICBM template brain (2009c) for channel visualization is publicly available at https://nist.mni.mcgill.ca/icbm-152-nonlinear-atlases-2009/.

Research involving human participants, their data, or biological material

Policy information about studies with human participants or human data. See also policy information about sex, gender (identity/presentation), and sexual orientation and race, ethnicity and racism.

Reporting on sex and gender	Due to limited sample size, gender was not considered as a variable of interest in the experiment design, and we did not analyze its effect on behavioral and neural results. However, our dataset was not severely biased regarding patient gender (19 males out of 31 for the whole dataset, and 16 males out of 25 for the neural dataset), and our results showed consistent patterns across individuals, dyads or groups, indicating the findings are applicable to both genders.
Reporting on race, ethnicity, or other socially relevant groupings	No socially constructed or relevant grouping variable was used and reported in the manuscript. We did not take these variables into account in the experimental design because of the limited sample size. Participant dyad gender or age did not show a significant impact on our behavioral results. In the main task, to control for opponents' potential impact on the behavioral results, we included the percentage of maintenance period of the competing team as a covariate when conducting ANOVAs (Supplementary Table 5). We also clarify that the aim of the 4-person task was to replicate the main results observed in the 2-person task. The impact of team size (2- or 4-person teams) and the type of collective goals (competitive or non-competitive goals) on cooperation dynamics was not a major focus of the current study.
Population characteristics	Twenty-one epilepsy patients (19 males, age = 25.8 ± 9.2 years old, demographic details in Supplementary Table 1) participated in this study. All patients were implanted with intracranial depth electrodes and were undergoing iEEG recording to locate the seizure onset zone, with electrode placement determined exclusively based on clinical requirements. All participants recruited for this study had no history of psychiatric disorders, head trauma, or encephalitis. The neural dataset consisted of eighteen patients (16 males, age = 27.5 ± 9.0 years old), who had electrodes implanted in the amygdala, TPJ contralateral to or outside of the epileptogenic zone. Prior to participation, all participants provided informed consent and were acknowledged their right to withdraw at any time during the study. Participants received compensation for their participation.
Recruitment	1. Two or more patients that underwent iEEG monitoring at the same time (e.g., in the same hospital room) after electrode implantation became potential participants of our study. The access to the patients was granted by the three ethical committees described below. They were recruited regardless of the location of the electrodes in order to avoid any bias. As with all iEEG studies involving epilepsy patients, all patient participants were from a pool of similarly impacted non-neurotypical subjects with severe degrees of epileptic activity, which may have potential impact on the task performance and the interpretation of neural data. The removal of bad channels and interictal epileptiform discharges were employed in order to reduce the potential impact from epileptic activity. 2. Healthy participants in this study were recruited as paid volunteers via on campus flyer recruitment or an online recruitment system. There was no potential self-selection bias in the participant recruitment.
Ethics oversight	The experimental protocols were in accordance to the latest version of the Declaration of Helsinki and received approval from local Institutional Review Board at each hospital (i.e., Chinese PLA General Hospital, S202139402; Beijing Xuanwu Hospital, ClinRes No. 2022018; Beijing Tiantan Hospital, KY 202008002).

Note that full information on the approval of the study protocol must also be provided in the manuscript.

Field-specific reporting

Please select the one below that is the best fit for your research. If you are not sure, read the appropriate sections before making your selection.

☒ Life sciences ☐ Behavioural & social sciences ☐ Ecological, evolutionary & environmental sciences

For a reference copy of the document with all sections, see nature.com/documents/nr-reporting-summary-flat.pdf

Life sciences study design

All studies must disclose on these points even when the disclosure is negative.

Sample size	Similar to the majority of iEEG studies (ref58-64), we did not conduct a prior sample size estimation. Our sample size for single brain analysis

Sample size	was comparable to or larger than those reported in most of previous iEEG publications (ref58,62-64). For individual-level analyses, numbers of clean channel in regions of interest (amygdala: 169 channels, TPJ: 258 channels) were similar to or larger than those reported in other iEEG publications (ref62,63,65,66). For dyad-level analyses, the numbers of dyads and channel-pairs (Supplementary Table 2) were comparable to those reported in animal studies examining inter-brain correlation (ref50,51), since there was no existing hyper-iEEG study conducted on humans. Moreover, our main findings are statistically highly significant and robust across individual participants or dyads while surviving multiple comparison correction.
Data exclusions	1. Behavioral: We performed several quality checks on the behavioral data to eliminate noises and extreme values in our following analysis: i) replacing time points with a velocity magnitude above the 99th quantile across all sessions with null values; ii) removing data within a 1-s time-window around reset points to minimize the impact of unstable movements during reset events when we analysized profiles of the initiation state rather than the transitions time-window; iii) removing data within the 1-s time-window around between-state transitions when we performed the behavioral-neural correlation analysis. 2. Neural: Four patients were excluded from neural analysis as they did not have electrodes implanted in the amygdala or TPJ contralateral to or outside of the epileptogenic zone. Channels underwent a quality check and were labeled as bad channels and discarded if they met any of the following criteria (ref60): i) located within the epileptic zone or severely contaminated by epileptic activity by visual inspection of the power spectrum; ii) variance greater than three times the mean variance across all channels during the entire task session. This step was repeated until no more bad channels were detected by the algorithm. All remaining channels were further visually inspected. Furthermore, iEEG signals were identified as IEDs (interictal epileptiform discharges) if they met either of the following criteria and were subsequently excluded from further analyses (ref76): i) the envelope of the unfiltered signal was four standard deviations (SDs) away from the baseline (i.e., the average of the entire time series); ii) the envelope of the filtered signal (band-pass filtered at 25-80 Hz) was five SDs away from the baseline. These steps were repeated until no more IEDs could be identified. Interictal spikes defined as 100μV changes between successive samples (ref60) were also detected and labeled as IEDs. Additionally, we smoothed detected IEDs by including an 800-ms time-window around each IED (400ms before and after), which was then discarded in all subsequent analyses. We omitted epochs containing IEDs when analyzing initiation and maintenance epochs. Finally, we visually inspected all channels for IEDs and removed those with excessive remaining artifacts.
Replication	1. We analyzed the main behavioral and neural results on the individual/dyad level and found strikingly consistent patterns in individuals/dyads across sessions. 2. Furthermore, we conducted a replication task, which is a modified version of the main task to assess the generalization of our main findings in a context that involved no competition and more teammates. The main findings from the 2-person dynamic cooperation task were replicated in the non-competitive settings of 4-person team, suggesting the robustness of the results regardless of team size (e.g., 2- or 4-person teams) and the type of collective goals (e.g., competitive or non-competitive goals). The analysis methods and results for the main task and replication task are reported in the manuscript (main figures and Extended Data Fig. 7 and 8).
Randomization	In the main task, we recruited four participants, either four patients or two patients and two healthy participants. Patients were paired as 2-person teams. When only two patients were recorded simultaneously, two healthy participants were paired as a team to play with the patient team. No experimental conditions were designed in the task. Therefore, randomization of experimental conditions or stimulus presentation were not relevant in the current study.
Blinding	Experimenters were not blinded with regards to the group identity (i.e., patient or healthy dyad) in both tasks. No experimental conditions are designed in the task. Therefore, blinding of experimental conditions was not relevant during data collection or analyses.

Behavioural & social sciences study design

All studies must disclose on these points even when the disclosure is negative.

Study description	
Research sample	
Sampling strategy	
Data collection	
Timing	
Data exclusions	
Non-participation	
Randomization	

Ecological, evolutionary & environmental sciences study design

All studies must disclose on these points even when the disclosure is negative.

Study description	
Research sample	

Sampling strategy	
Data collection	
Timing and spatial scale	
Data exclusions	
Reproducibility	
Randomization	
Blinding	

Did the study involve field work? ☐ Yes ☐ No

Field work, collection and transport

Field conditions	
Location	
Access & import/export	
Disturbance	

Reporting for specific materials, systems and methods

We require information from authors about some types of materials, experimental systems and methods used in many studies. Here, indicate whether each material, system or method listed is relevant to your study. If you are not sure if a list item applies to your research, read the appropriate section before selecting a response.

Materials & experimental systems

n/a	Involved in the study
☒	☐ Antibodies
☒	☐ Eukaryotic cell lines
☒	☐ Palaeontology and archaeology
☒	☐ Animals and other organisms
☒	☐ Clinical data
☒	☐ Dual use research of concern
☒	☐ Plants

Methods

n/a	Involved in the study
☒	☐ ChIP-seq
☒	☐ Flow cytometry
☐	☒ MRI-based neuroimaging

Antibodies

Antibodies used	
Validation	

Eukaryotic cell lines

Policy information about cell lines and Sex and Gender in Research

Cell line source(s)	
Authentication	
Mycoplasma contamination	
Commonly misidentified lines (See ICLAC register)	

Palaeontology and Archaeology

Specimen provenance	
Specimen deposition	
Dating methods	

☐ Tick this box to confirm that the raw and calibrated dates are available in the paper or in Supplementary Information.

Ethics oversight	

Note that full information on the approval of the study protocol must also be provided in the manuscript.

Animals and other research organisms

Policy information about studies involving animals; ARRIVE guidelines recommended for reporting animal research, and Sex and Gender in Research

Laboratory animals	
Wild animals	
Reporting on sex	
Field-collected samples	
Ethics oversight	

Note that full information on the approval of the study protocol must also be provided in the manuscript.

Clinical data

Policy information about clinical studies

All manuscripts should comply with the ICMJE guidelines for publication of clinical research and a completed CONSORT checklist must be included with all submissions.

Clinical trial registration	
Study protocol	
Data collection	
Outcomes	

Dual use research of concern

Policy information about dual use research of concern

Hazards

Could the accidental, deliberate or reckless misuse of agents or technologies generated in the work, or the application of information presented in the manuscript, pose a threat to:

No	Yes	
☐	☐	Public health
☐	☐	National security
☐	☐	Crops and/or livestock
☐	☐	Ecosystems
☐	☐	Any other significant area

Experiments of concern

Does the work involve any of these experiments of concern:

No	Yes	
☐	☐	Demonstrate how to render a vaccine ineffective
☐	☐	Confer resistance to therapeutically useful antibiotics or antiviral agents
☐	☐	Enhance the virulence of a pathogen or render a nonpathogen virulent
☐	☐	Increase transmissibility of a pathogen
☐	☐	Alter the host range of a pathogen
☐	☐	Enable evasion of diagnostic/detection modalities
☐	☐	Enable the weaponization of a biological agent or toxin
☐	☐	Any other potentially harmful combination of experiments and agents

Plants

Seed stocks

Novel plant genotypes

Authentication

ChIP-seq

Data deposition

☐ Confirm that both raw and final processed data have been deposited in a public database such as GEO.

☐ Confirm that you have deposited or provided access to graph files (e.g. BED files) for the called peaks.

Data access links
May remain private before publication.

Files in database submission

Genome browser session
(e.g. UCSC)

Methodology

Replicates

Sequencing depth

Antibodies

Peak calling parameters

Data quality

Software

Flow Cytometry

Plots

Confirm that:

☐ The axis labels state the marker and fluorochrome used (e.g. CD4-FITC).

☐ The axis scales are clearly visible. Include numbers along axes only for bottom left plot of group (a 'group' is an analysis of identical markers).

☐ All plots are contour plots with outliers or pseudocolor plots.

☐ A numerical value for number of cells or percentage (with statistics) is provided.

Methodology

Sample preparation	
Instrument	
Software	
Cell population abundance	
Gating strategy	

☐ Tick this box to confirm that a figure exemplifying the gating strategy is provided in the Supplementary Information.

Magnetic resonance imaging

Experimental design

Design type	MRI was used only to determine the localization of electrode contacts within the brain. Participants did not perform any experimental task during MRI scanning.
Design specifications	No experimental design was used during MRI scanning.
Behavioral performance measures	No behavioral data was collected during MRI scanning.

Acquisition

Imaging type(s)	Structural
Field strength	3 Tesla
Sequence & imaging parameters	Pre-implant structural T1-weighted scans were obtained using magnetization-prepared rapid gradient echo sequence with standard parameter settings.
Area of acquisition	Whole brain scan was used.

Diffusion MRI ☐ Used ☒ Not used

Preprocessing

Preprocessing software	Structural image were preprocessed using FieldTrip (v20220310) for alignment of ACPC (Anterior Commissure - Posterior Commissure) coordinate system and then reconstructed using the 'recon-all' function in Freesurfer (v5.3.0).
Normalization	Structural image was normalized to using SPM12 to obtain deformation parameters that transform electrode positions from patients' native space to standard MNI space
Normalization template	Default tissue probability map in SPM12.
Noise and artifact removal	No noise or artifact removal procedures were applied.
Volume censoring	No volume censoring were applied.

Statistical modeling & inference

Model type and settings	No task-related model-based analysis was performed using MRI data.

Effect(s) tested: No model-based analysis was performed using MRI data.

Specify type of analysis: ☐ Whole brain ☐ ROI-based ☐ Both

Statistic type for inference (See Eklund et al. 2016): No statistical analysis was performed using MRI data.

Correction: No statistical correction for multiple comparisons was used for MRI data.

Models & analysis

n/a	Involved in the study
☒	☐ Functional and/or effective connectivity
☒	☐ Graph analysis
☒	☐ Multivariate modeling or predictive analysis

Functional and/or effective connectivity:

Graph analysis:

Multivariate modeling and predictive analysis: